ACS NANO

www.acsnano.org

Bottom-Up Assembled Photonic Crystals for Structure-Enabled Label-Free Sensing

Juan Wang,* Pepijn W. H. Pinkse, Loes I. Segerink, and Jan C. T. Eijkel

Cite This: *ACS Nano* 2021, 15, 9299−9327

ABSTRACT: **Photonic crystals (PhCs) display photonic stop bands (PSBs) and at the edges of these PSBs transport light with reduced velocity, enabling the PhCs to confine and manipulate incident light with enhanced light−matter interaction. Intense research has been devoted to leveraging the optical properties of PhCs for the development of optical sensors for bioassays, diagnosis, and environmental monitoring. These applications have furthermore benefited from the inherently large surface area of PhCs, giving rise to high analyte adsorption and the wide range of options for structural variations of the PhCs leading to enhanced light−matter interaction. Here, we focus on bottom-up assembled PhCs and review the significant advances that have been made in their use as label-free sensors. We describe their potential for point-of-care devices and in the review include their structural design, constituent materials, fabrication strategy, and sensing working principles. We thereby classify them according to five sensing principles: sensing of refractive index variations, sensing by lattice spacing variations, enhanced fluorescence spectroscopy, surface-enhanced Raman spectroscopy, and configuration transitions.**

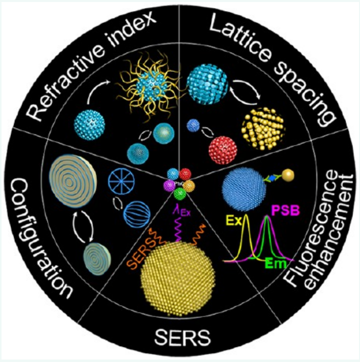

KEYWORDS: *photonic crystals, photonic stop band, slow light, self-assembly, optical label-free sensor, signal readout, sensitivity, limit of detection*

INTRODUCTION

Photonic crystals (PhCs) have been widely applied in fields of energy conversion,[1] light harvesting,[2] displays,[3] information encryption,[4] anticounterfeiting,[5] and sensing.[6] Their popularity can be attributed to their convenient, precisely controllable, and flexibly tunable fabrication by self-assembly from a nanoscale building block assembly approach[7] and their specific optical properties, namely, their photonic stop bands (PSBs) and the slow light effect.[8,9] Some previous reviews have discussed PhC fabrication[5] and applications for sensing,[10] anticounterfeiting,[5] and light harvesting.[2] Although the use of stimuli-responsive PhCs for chemical and/or biological sensing of solvents, vapors, chemical compounds, and biomolecules has been fully discussed by Fenzl and co-workers[10] from one-dimensional (1D) to three-dimensional (3D) PhCs, the optical readout scheme was limited to reflection and diffraction shifts. In this review, we broaden the optical readout schemes from diffraction shifts to enhanced fluorescence spectroscopy, surface-enhanced Raman spectroscopy (SERS), and configuration transitions with the aim of optimizing the sensing performance in terms of sensitivity and limit of detection (LoD). We mainly focus on PhCs assembled by a bottom-up approach from constituent building blocks and their use for point-of-care (POC) devices for label-free chemical and/or biological sensing.

Among the many sensing principles and their associated materials, such as electrochemical sensors using functional nanomaterials,[11] photoluminescence sensors using quantum dots,[12] and optical sensors using nanostructured nanophotonics,[13−16] optical sensors employing PhCs stand out as their periodic structures, and thus their corresponding optical properties can be precisely controlled. The precise control enables label-free, noninvasive, and multiplexed analysis. Hereby especially the PhCs assembled from colloids stand out. The bottom-up approach of colloid self-assembly allows their low-cost manufacturing with high efficiency and high-resolution structures.

To outline the advantages of PhC sensors, a brief comparison can be made with electrochemical and photoluminescent sensors. Electrochemical sensors transfer a specific recognition event to a relevant electric signal by measurement of current, potential, or conductance. Researchers have turned to engineering nanomaterials (from zero-dimensional (0D) to

Received: March 23, 2021
Accepted: May 19, 2021
Published: May 24, 2021

https://doi.org/10.1021/acsnano.1c02495
ACS Nano 2021, 15, 9299−9327

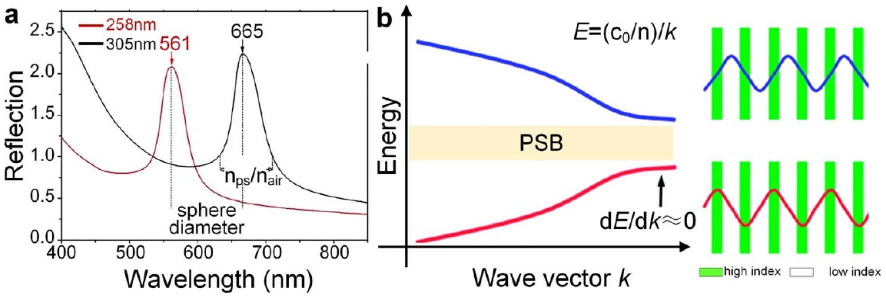

Figure 1. Optical properties of the PhCs. (a) Reflection spectra with tunable PSBs by control over the size of the PhC building blocks. The PhCs are assembled polystyrene nanoparticles of 258 nm (red curve) or 305 nm (black curve) diameter. Adapted from ref 9. Copyright 2012 American Chemical Society. (b) Simplified dispersion diagram of a PhC, showing the energy (E) of a photon *vs* the wave vector k, featuring a PSB. Alternating green−white lines represent the periodic structure of the PhCs, where green indicates a high index of refraction, while white indicates a low index of refraction. At the red edge of the PSB, the absolute value of the light field peaks in the dielectric regions with high refractive index (red curve), while at the blue edge of the PSB, the peaks in regions with low refractive index (blue curve). Reproduced from ref 29. Copyright 2003 American Chemical Society.

3D) and nanostructures (from arrays to hybrid structures/materials) to improve their sensitivity and selectivity. For example, the catalytic activity of noble metal nanomaterials/nanostructures can improve signal generation and amplification.[17] However, it is still challenging to implement a multiplexed analysis with high sensitivity. Therefore, a labeling strategy is often employed to improve the sensitivity and lower the LoD when a label-free approach is not be feasible or sufficiently sensitive for a chosen transduction principle.[11] Labeling, however, represents a complicating extra step. The photoluminescent approach leverages the Förster resonance energy transfer (FRET) and electron/charge transfer for biosensing using, for example, quantum dots (QDs).[12] However, the QDs suffer from a low quantum yield, influencing the detection sensitivity. Considering their combination of high sensitivity and high selectivity, PhCs offer promising alternatives to electrochemical sensors and FRET-based sensors.

PhC-based optical sensors provide easy opportunities for structure modification to obtain strong and specific analyte adsorption but can also serve as barcodes as each PhC can have its own characteristic spectrum due to Bragg diffraction, which is regulated by the size of the building blocks. These barcodes can be tailored in a wide visible spectral region and are very stable, enabling multiplexed assays. This forms an advantage compared to fluorescent dyes, carbon dots (CDs), and QDs.[18] Additionally, PhCs are transducers with enhanced optical signal readout. On the basis of these considerations, this review is organized as follows. We first discuss the optical properties of PhCs and subsequently the label-free PhC-based sensing applications. We have classified these label-free PhC-based sensing methods according to their working principles, which can be Bragg diffraction shifts (in response to changes of refractive index and lattice spacing), enhanced fluorescence spectroscopy, SERS, and configurational changes. For each of these working principles, we highlight and discuss the sensor structural design, constituent materials, fabrication strategy, detectable target analytes, as well as detection sensitivity and LoD.

In time, we expect that the research investigations of PhC-based label-free sensing will lead to the development of rapid and user-friendly portable devices for POC diagnosis and *in situ* detection that provides a fast response, a high sensitivity, and low LoD.[19] We aim to offer insights in this review that can stimulate further scientific/technological advancements in on-demand label-free PhC sensors benefiting the fields of bioassays, diagnosis, and environmental monitoring.

OPTICAL PROPERTIES OF PhCs

PhCs are periodic structures of constituents with alternating dielectric constants on a length scale comparable to the wavelength of light, preventing light from propagating in certain directions at specific frequencies.[20,21] As a result, they produce PSBs and show structural colors.[22] The specific structural color of each PhC can serve as label-free photonic code, which is highly useful to enable PhCs to serve as sensing units for high-throughput detection.[23,24] This photonic code can be precisely controlled by the size of the PhC building blocks (Figure 1a).[25] Note that the dimension of the used PhCs in this work is generally larger than 100 μm, and the optical behavior is closer to the case of the infinite periodic structure. Thus, the size of the building blocks determines the Bragg peak position, and $n_{\mathrm{PS}}/n_{\mathrm{air}}$ mainly determines the diffraction peak width. The reflection intensity becomes saturated once the number of alternating periodic layers surpasses a threshold value.[20,26] The PSB of PhCs can be estimated by the Bragg−Snell law (more details will be presented in the section of Refractive Index Variation-Induced Sensing). At the edges of the PSBs, the density of states (DOS) is significantly enhanced with an increase in both energy density and residence time. Therefore, light can travel with a reduced group velocity, which is denoted as slow light effect.[8] At the red edge of the PSBs, the light standing wave is localized in regions with high refractive index, while at the blue edge of the PSBs, it is localized in regions with low refractive index, as shown in Figure 1b. Also, because of the vanishing DOS, any electromagnetic (EM) wave in the PSBs is evanescent. Thus, by tailoring resonances of the PSBs and the integrated emitters confined in PhC structures, the light−matter interaction[27] can be enhanced for applications in enhanced fluorescence spectroscopy and SERS with improved sensitivity and lower LoD.[28]

PhCs ASSEMBLED FROM BUILDING BLOCKS APPLIED AS CHEMICAL/BIOLOGICAL LABEL-FREE SENSORS

Optical sensors constructed from PhCs have been widely explored in fields of diagnosis, bioassays, and environmental monitoring owing to the exquisite tunability of their optical properties. Compared to optical sensors made by a top-down approach of either metals (*e.g.*, plasmonic structures)[30] or dielectrics (*e.g.*, dielectric metasurfaces),[31] the bottom-up assembly[32] from colloids allows the facile fabrication of a wide variety of PhCs with the advantages of low cost, high efficiency, and high structural resolution (down to a few nanometers).[33] Furthermore, PhC structures can be easily exposed to liquids and integrated in microfluidic devices to benefit the development of POC devices.

Suspension barcodes (*e.g.*, fluorescent particles,[34] semiconductor QDs,[35] plasmonic nanoparticles,[36] and PhC beads[37]) have become increasingly popular in sensing to create multiplexed assays with high throughput.[36] Among these barcodes, PhCs consisting of periodic structures assembled by building blocks of, *e.g.*, polystyrene nanoparticles (PSNPs), silica nanoparticles (SiO_2NPs), or nematic liquid crystals (NLCs), as well as cellulose nanocrystals (CNCs) have a combination of properties. They are self-encoded carriers with high specific surface area and flexibility in probe immobilization and also can serve as useful labels for a multiplexed assay. As a label, they possess high encoding stability, high visibility by optical microscopy or the naked eye, and they cause fluorescence signal enhancement and show a high resistance to photobleaching and freedom of any fluorescent background.[36,37] When the PhCs are used as sensors, they provide a facile manner of transducing various external stimuli into readily measurable optical readouts by low-cost photodetectors, digital cameras, or even the naked eye.[38,39] A variety of PhC structures, including periodic close-packed opal structures, inverse opal structures, core–shell structures, and Janus structures, have been developed as label-free sensing units with high sensitivity and low LoD. These PhC-based sensors can be classified by their various working mechanisms, such as refractive index change sensing, lattice variation-induced sensing, enhanced fluorescence sensing, SERS-based sensing, and configuration transition-induced sensing. Figure 2 shows a schematic diagram of these different sensing mechanisms of PhCs, including refractive index-induced variation and lattice spacing change, which can both be monitored by the Bragg diffraction spectra or by color shifts. In addition, PhCs have been used for amplification of optical signal readout in enhanced fluorescence spectroscopy and for SERS due to the enhanced light–matter interaction. Finally, we reviewed PhCs with a sensing function based on configurational changes. Table 1 summarizes the PhC-based sensors according to these various working mechanisms, emphasizing their structural design, constituent materials, fabrication method, target analytes, sensitivity, and LoD.[39]

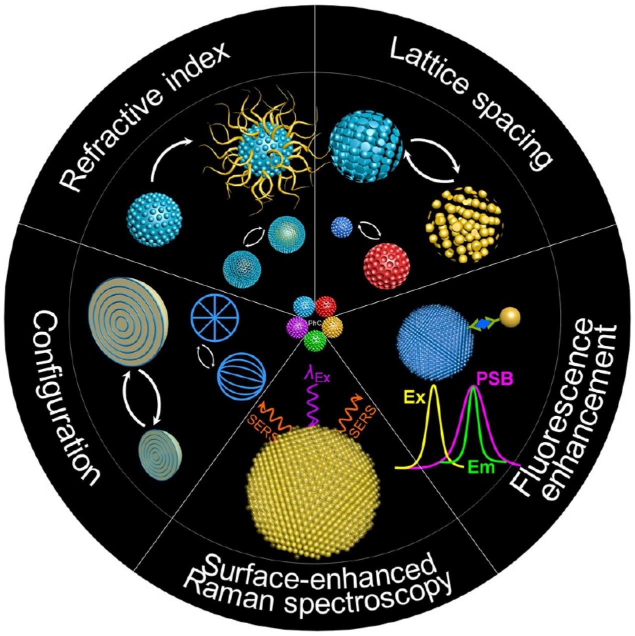

Figure 2. Schematic diagram of PhC-based sensors classified by their sensing mechanism as discussed in this review. Ex and Em represent the excitation frequency and emission frequency.

REFRACTIVE INDEX VARIATION-INDUCED SENSING

The optical properties of PhCs can be estimated by band calculations with respect to a specific angle of incidence.[21] The bottom-up colloid assembly normally leads to face-centered cubic (fcc) or hexagonal close-packed (hcp) structures with the (111) crystalline plane being parallel to the substrate.[32] Thus, the observed PSB at normal incidence is a result of the Bragg diffraction peak of the (111) plane of the PhCs, which can be approximately calculated by the Bragg–Snell law[9,76]

$$m\lambda = \sqrt{\frac{8}{3}}D\sqrt{{n_{\mathrm{eff}}}^2 - \sin^2\theta} \tag{1}$$

indicates that changes in average refractive index (n_{eff}) of the PhCs, lattice spacing (D), as well as angle of light incidence with respect to the normal (θ) can give rise to Bragg diffraction shifts, where m is the order of diffraction and λ is the wavelength of the diffraction peak. A PhC structure consists of periodic dielectric nanoparticles with a dielectric medium, namely, air, solvent, hydrogels, or precursors, and D then is the diameter of the building blocks. The n_{eff} of PhCs can be approximately calculated by[77]

$$ {n_{\mathrm{eff}}}^2 = {n_{\mathrm{p}}}^2 V_{\mathrm{p}} + {n_{\mathrm{m}}}^2 V_{\mathrm{m}} \tag{2}$$

Here, n_{p} and n_{m} are the refractive indices of the constituent particles and surrounding medium, respectively, and V_{p} and V_{m} are their corresponding volume fractions. Thus, such tunable optical properties of PhCs can enable them to be applied as sensing units due to their response in structural color when the n_{eff} of a PhC structure changes, which can be readily distinguished by our naked eye or a microscope with an optical spectrometer. Note that this is especially applicable to 3D PhCs as they can have PSBs in all directions with wide viewing angle properties.[4,37,78] The change of structural color will then not be influenced by variations in the angle of light incidence with respect to the normal.

Homogenous PhC structures assembled from solid building blocks such as SiO_2NPs or PSNPs, which are also termed opal structures, normally show a hcp arrangement with volume fractions of the solid building blocks of 0.74 and air voids of 0.26.[25] On the contrary, the inverse opals, which can be replicated from the opal structures, show volume fractions of the air voids of 0.74 and of the solid matrix of 0.26. Figure 3 shows schematic and scanning electron microscopy (SEM) close-up images of the opal and inverse opal structures. For sensing purposes, the inverse opals have become more popular owing to the large volume available for analyte filling, and the high surface area for analyte adsorption, causing a higher refractive index change. Recently, a variety of opal/inverse opal structures have been developed for sensing by their response to external stimuli and changes in their local environment with

Table 1. PhC-Based Sensors by Their Working Mechanisms[a]

sensing mechanism	analytes	PhC structure	constituent materials	fabrication method	selectivity mechanism	LoD	refs
refractive index	small molecules	silk-fibroin-based inverse opal film	silk matrix	PSNP assembly, silk casting, and PS dissolution	solubility	isopropyl alcohol−glycerol mixtures: 263 nm/RIU	40
		molecularly imprinted polymers (MIP) on inverse opal film	benzocaine-imprinted hydrogel	vertical assembly and molecular imprinting	MIP	benzocaine: 0.1 mM	41
	glycoproteins	inverse SPCs	ultrafine SiO_2NP matrix	droplet confinement-induced assembly and inversion	probe immobilization	*e.g.,* human CA19-9: 50 U·mL^{-1}	42
		MIP-immobilized inverse SPCs	polyacrylamide (PAM) matrix			bovine Hb: 1 ng·mL^{-1}	43
		mesoporous SiO_2 opals	alkoxysilanes-functionalized mesoporous SiO_2NPs	droplet confinement-induced assembly	alkolysilane labels	ethanol: 600 ppm	44
	vapor	inverse SiO_2 opal film	polymer infiltrated SiO_2 inverse opals	coassembly and infiltration	solubility	*o*-xylene: 0.51 μg·mL^{-1} *m*-xylene: 0.41 μg·mL^{-1} *p*-xylene: 0.17 μg·mL^{-1}	45
lattice spacing	ions	metal−organic framework (MOF)-coated monolayer PhC	PSNPs with MOF layer	PSNP assembly and *in situ* crystallization	MOF size exclusion and molecular interaction	*e.g.,* acetonitrile ∼5000 ppm	46
		opal film in hydrogel matrix	8-hydroxyquinoline (HQ) functionalized hydrogel matrix	self-assembly, infiltration and functionalization	metal−ligand binding	Cu^{2+}: 10^{-21} M	47
		photonic cholesteric liquid crystals (CLC) polymer film	benzoic acid functionalized CLC polymers	CLC polymerization	benzoic acid binding-site-induced dehydration	Ca^{2+}: 10^{-4} M	48
		inverse opal polyelectrolyte films	ion-sensitive polyelectrolyte as matrix	opal self-assembly, matrix polymerization, and functionalization	solvation and Donnan potential	*e.g.,* arginine: 10^{-4} M	49
	small molecules	opal film in hydrogel matrix	enzyme (CD)- and titrating group (2NPh)- modified hydrogel matrix	self-assembly and post polymerization	enzyme reaction	creatinine: 6×10^{-6} M	50
		MIP-immobilized inverse SPCs	PMMA hydrogel as matrix	droplet-induced assembly, molecular imprinting, polymerization, and SiO_2 extraction	MIP	methanephosphonic acid: 10^{-6} M	51
		poly(ionic liquid) inverse SPCs	poly(ionic liquid) as matrix	droplet confinement-induced assembly, poly(ionic liquid) infiltration, and SiO_2 etching	hydrogen bonding	nitrate explosives: 5−10 μM	52
	protein	opal film in hydrogel matrix	antibody/antigen-immobilized hydrogels as matrix	PSNPs self-assembly and polymerization	competitive antibody−antigen interaction	*e.g.,* protein A: 5 μg·mL^{-1}	53
	nucleic acid	inverse hydrogel SPCs	probe-immobilized hydrogel as matrix	droplet microfluidics and probe modification	specific hybridization	DNA: 10^{-9} M	38
	local environment	nanohydrogel opal film	smart nanogel as building blocks	vertical deposition	hydrogen bond interaction	relative humidity (20−100%)	54
		photonic microcapsules	microcapsules containing smart nanogel colloids	droplet confined assembly by depletion attraction	thermal-responsive property of PNIPAM	temperature (25−40 °C)	55
enhanced fluorescence spectroscopy	metal ions	PS bead opal films and SPCs	8-HQ and polyvinylpyrrolidone infiltrated PS arrays	vertical deposition and functional species infiltration	Fluorescence enhancement and quenching effect	*e.g.,* Cu^{2+}, Al^{3+}: 10^{-11} M	56
	nucleic acid	poly(styrene-methyl methacrylate-acrylic acid) (poly(St-MMA-AA)) opal film	probe-immobilized poly(St-MMA-AA)NPs	self-assembly and probe immobilization	hybridization and FRET	DNA: 1.35×10^{-14} M	57
		core (opal)-shell (inverse opal) SPCs	probe-immobilized porous hydrogel shell and solid SiO_2NP lattice core	droplet confinement-induced self-assembly and controlled etching	rolling cycle amplification	miRNA: 2×10^{-14} M	58
	glycoproteins	probe-decorated inverse opal SPCs	probe-immobilized hydrogel as matrix		antigen−antibody recognition	inflammatory cytokines: ∼10 ng·mL^{-1}	59
		core (opal)−shell (inverse opal) SPCs	shell: hybrid hydrogel of poly((ethylene glycol) diacrylate (PEGDA) and gelatin core: SiO_2NP lattice			cardiac troponin I: 0.009 ng·mL^{-1} B-type natriretic peptide: 0.084 pg·mL^{-1} myoglobin: 0.68 ng·mL^{-1}	60

Table 1. continued

sensing mechanism	analytes	PhC structure	constituent materials	fabrication method	selectivity mechanism	LoD	refs
SERS	enzyme	superwettable patterned opal film	aptamer functionalized SiO_2 opals	hydrophobic–hydrophilic patterning and NP self-assembly	hybridization	thrombin: 1.8×10^{-13} M	61
	small molecules	metallo-dielectric coated PhCs	PSNPs as building blocks integrated with Si/Ag alternating layers	self-assembly and metal deposition		R6G: 10^{-11} M	62
		inverse metallic opals	metal (Ag, Cu, Ni, Co) as matrix	PSNP template self-assembly, electrochemical deposition, and PS dissolution		R6G: 10^{-13} M	63
		inverse TiO_2 opal film	TiO_2 as matrix	PSNP self-assembly, TiO_2 casting, and calcination		methylene blue: 6×10^{-6} M	64
		artificial copper butterfly wing	3D Cu structure	sol–gel CuO deposition, wing calcination, CuO reduction		DNA bases: $\sim 10^{-6}$ M	65
	antigens	AuNP-decorated SPCs	SiO_2NP lattice with antibodies	droplet confinement-induced self-assembly and antibody immobilization	Raman tagged antibody/antigen sandwich	mouse IgG: 9.2 pg·mL^{-1} CEA: 1.3 pg·mL^{-1} AFP: 4.8 pg·mL^{-1}	66
		Au@Ag incorporated inverse hydrogel opal SPCs	PAM as hydrogel matrix	droplet confinement-induced PSNP self-assembly, PAM infiltration, PS dissolution, and antibody immobilization		CEA: 1.9 fg·mL^{-1} AFP: 3.6 fg·mL^{-1}	67
configuration transition	metal ions	stearic-acid-decorated 5CB droplets	5CB	drop-casting	interaction between metal ions and deprotonated carboxylate moiety	Co^{2+}: 50 pM; Cu^{2+}: 30 pM	68
		PAA interpenetrated CLC sphere	RM727 and PAA	droplet microfluidics, photopolymerization, chiral dopant extraction, and polymer infiltration		Ca^{2+}: μM	69
	small molecules	(PAA-b-LCP)-coated CLC droplets	MLC-2132 doped with chiral dopant	droplet microfluidics, immobilization of PAA, glucose oxidase or cholesterol oxidase	enzyme label	glucose: 5×10^{-7} M cholesterol: 2.5×10^{-6} M	70
	nucleic acid	PLL-coated NLC droplets	5CB/E7	layer-by-layer assembly	ionic charge interaction PLL/DNA	DNA: 5×10^{-8} M	71
	protein	phospholipid-coated NLC droplets	E7	droplet microfluidics, fusion with phospholipid liposomes	electrostatic interaction	antimicrobial peptides: $\sim 6 \times 10^{-6}$ M	72
	vapor	CLC film	E7 and dopants	surface coating and evaporation	vapor absorption	toluene: 48 ppm acetone: 28.7 ppm	73
		photonic chiral film	CNC with polyethylene glycol (PEG) and fluorescent molecule	coassembly		formaldehyde: 2 ppm	74
	solvent/humidity/temperature	polymerized CLC microspheres	NLC mesogen networked microparticle	droplet microfluidics of NLC mesogen and nonreactive chiral dopant, cross-linking, dopant extraction			75

[a] Above abbreviations of CEA: carcinoembryonic antigen, AFP: alpha fetoprotein, PLL: poly(L-lysine), PAA-b-LCP: poly(acrylicacid-b-4-cynobiphenyl-4-oxyundecylacrylate).

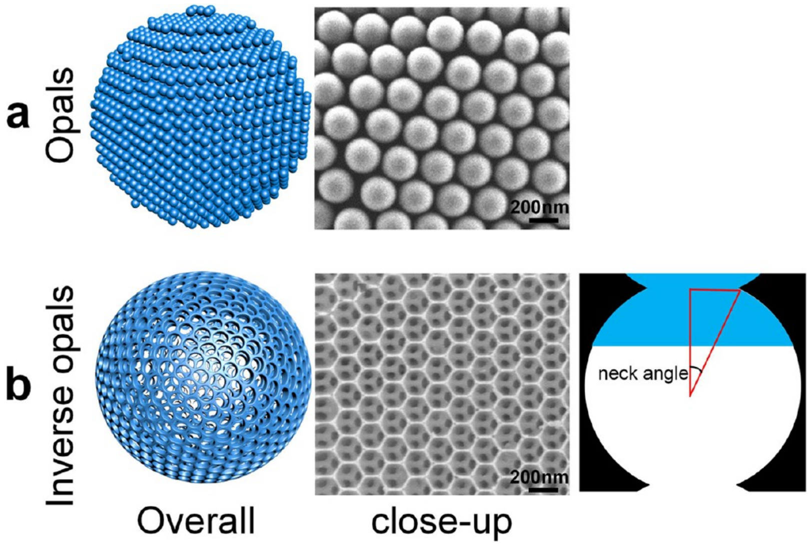

Figure 3. Schematic diagram and the corresponding SEM close-up images of the opal and inverse opal structures. (a) Opal PhC structure and (b) inverse opal PhC structure. The schematic in right panel shows the neck angle of the inverse opal structure, which determines the wettability of an inverse opal structure. The SEM image in (a) was adapted with permission from ref 4. Copyright 2020 Wiley. Panel (b) was reproduced from ref 84. Copyright 2011 American Chemical Society.

applications in detection of oil,[79] biomolecules,[80] proteins,[81] and volatile gas.[82,83]

The Song group has designed an oil-sensitive carbon inverse opal,[79] which can be applied as an oil sensor with a fast response in ~30 s with an obvious color change caused by the refractive index change when different oils adsorbed on the inverse opals (Figure 4a,(i)). The PSBs of the carbon inverse opals upon infiltration with different oils thereby show a linear shift when increasing the refractive index of the oils (Figure 4a,(ii)). Both the large PSB shift and the fast response can be ascribed to the large void volume fraction in the inverse opals. Furthermore, the responsiveness of the inverse opals will depend on the wettability of their constituent materials for the adsorbing oils with a good wettability facilitating the response by their structural color change. PhC structures have also been investigated for differentiation of water/ethanol mixtures[85,86] based on the difference in their wettability. The wettability of PhC structures can be well tuned by the number of layers of the periodic lattice, chemical surface coating, and neck angles (defined by the size of the pore diameter and the size of opening of the interconnected pores, as indicated in Figure 3b).[86] Therefore, such designs can achieve a fast visual identification.

Zhao *et al.*[42] demonstrated that inverse opal spheres can be applied for analysis of biomarkers (Figure 4b). Inverse opal spheres, compared to the two-dimensional (2D) arrays on a plate,[87] provide the advantage of higher diffusional analyte flux to bind with the probes due to the radial diffusion. This leads to a more efficient usage of samples and reagents. The inverse opal spheres were fabricated by microdroplet confinement-induced colloid crystallization of a lattice of PSNPs with diameters in the range of 200−300 nm as building blocks and ultrafine SiO_2NPs with average size smaller than 10 nm as matrix followed by a calcination process for removal of the PS lattices. The self-encoding properties with different PSBs could be tuned by the size of the PSNPs. As mentioned above, the porous lattices of inverse opal spheres improve the analyte binding efficiency because of the large specific surface area. Probe immobilization can furthermore achieve binding of specific targets to the differently encoded inverse opals. Figure 4b demonstrates the (i) PSB shifts as a function of biomarkers concentration and the (ii) capability for multiplexed immunoassays. The LoD of these designed inverse opal spheres for the human CA19-9 biomarker can reach 50 $U \cdot mL^{-1}$ with a ~1 nm PSB peak shift. The authors also demonstrated an optical response in a flow-through microchannel, which shows the potential of the structures for the development of POC devices with simplified equipment and procedures.

To further improve sensitivity and specificity, molecularly imprinted polymers (MIP) on hydrogel-based PhC structures have been introduced for biosensing.[41,43] In the MIP technique, MIPs are created with specific nanocavities which are complementary in geometry and functionality to the target molecules and therefore have high affinity for the targets. Such designed MIP-immobilized PhC structures show a sufficient Bragg diffraction shift (with 13.5 nm when saturated binding occurred), allowing identification even by the naked eye, benefiting from both the specific binding of target molecules inducing a refractive index change and the swelling of the MIP.[41,43] The maximum diffraction shift caused by the MIP hydrogel-based PhC structures is 2 times larger than the SiO_2-based inverse opals[42] (Figure 4b). Figure 4c(i) shows the fabrication principle of MIP inverse opals. The biomolecules were first immobilized onto the surface of opal microspheres featuring well-ordered SiO_2NP lattices (SiO_2NPs with diameter in a range of 200−300 nm). Then the hydrogel prepolymer (acrylamide solution) was infiltrated in the air voids of the opal microspheres and polymerized. Removal of the SiO_2NP lattices and preimmobilization of biomolecules yielded polyacrylamide inverse opal microspheres with amide groups and footprints of the imprinted biomolecules on the surface of the formed pores. When the MIP-immobilized inverse opals were exposed to the corresponding target analytes, it resulted in the formation of multiple hydrogen bonds, causing a strongly increased selective biomolecule binding affinity. A gradual Bragg diffraction peak shift to red spectral wavelengths can report this specific molecular binding with increasing concentration of target analytes. The LoD in

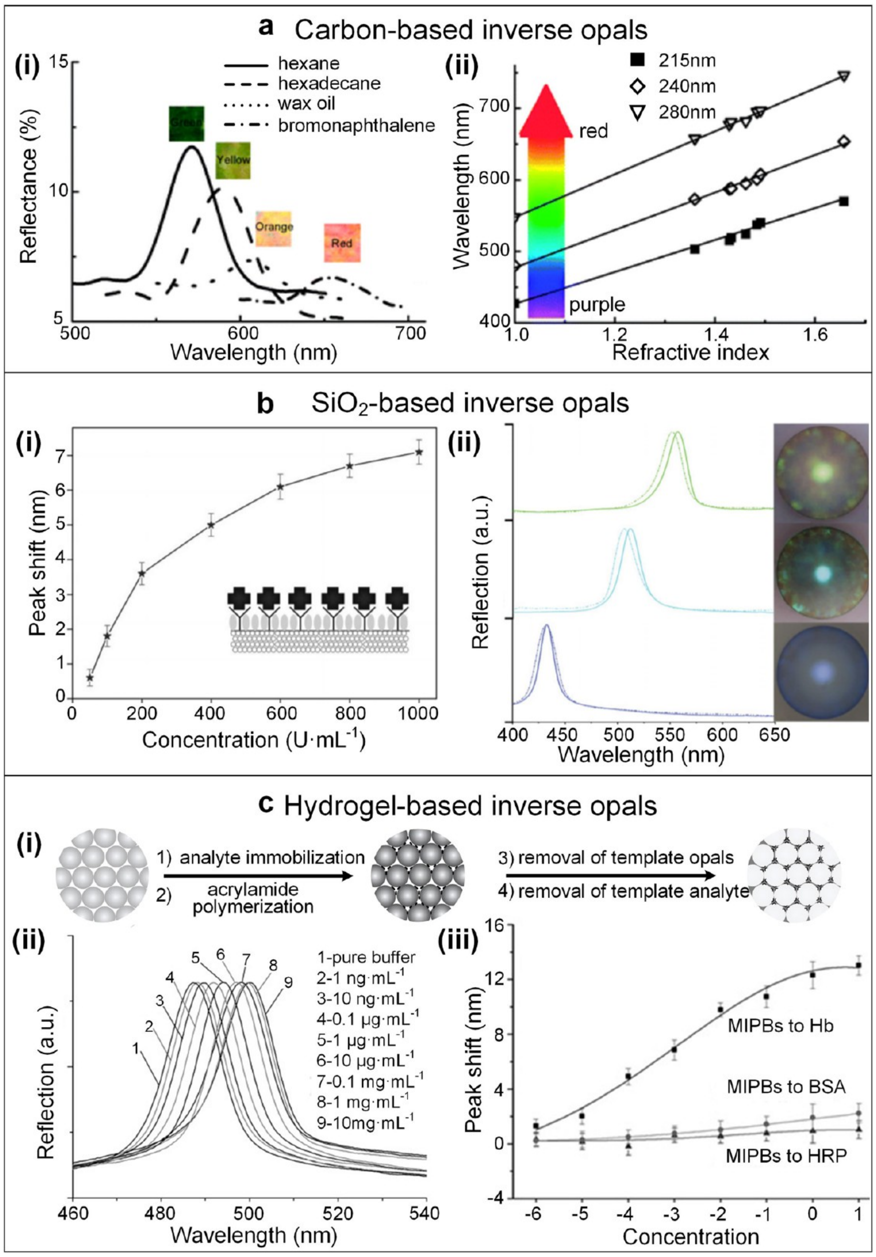

Figure 4. Refractive index variation-induced sensing by self-assembled PhCs. (a) Carbon-based inverse opals for oil sensing. (i) Reflection spectra and the optical microscopy images of carbon inverse opals upon infiltration with four different oils. (ii) PSB of the carbon inverse opals is a linear function of refractive indices. The pore diameters of the carbon-based inverse opals used are 215, 240, and 280 nm. Reproduced with permission from ref 79. Copyright 2008 Royal Society Chemistry. (b) SiO$_2$-based inverse opal spheres for biomarker detection. (i) Optical response to an increase in target concentration. (ii) Multiplex immunoassays using inverse opal spheres with different PSBs. Reproduced with permission from ref 42. Copyright 2009 Wiley. (c) Hydrogel-based MIP inverse opals for protein detection. (i) Diagram of the fabrication procedure of MIP-functionalized hydrogel inverse opals. (ii) Bragg diffraction response of bovine Hb-immobilized hydrogel inverse opals to varying concentration of bovine Hb. (iii) Specificity demonstration of the MIP-immobilized hydrogel inverse opals. The *x* axis of concentration is in logarithmic scale. Reproduced with permission from ref 43. Copyright 2009 Wiley.

these MIP-immobilized hydrogel-based inverse opals can reach 1 ng·mL^{-1} (∼32 pM), as shown in Figure 4c(ii). Figure 4c(iii) demonstrates the selectivity of hemoglobin (Hb)-imprinted MIP inverse opals with respect to bovine Hb, bovine serum albumin (BSA), and horseradish peroxidase (HRP) solution.

In addition to detection of targets in liquid phase, also targets in the vapor phase can be detected by the adsorbate-induced refractive index changes, either using functionalized opal structures[82] or inverse opal structures infiltrated with a functional polymer with high adsorption capacity for volatile vapor.[45,46,83] For example, an optical nose array chip consisting of mesoporous spherical photonic crystals (SPCs) functionalized with different alkoxysilanes was developed, showing an excellent discrimination among a wide range of compounds from the same chemical family and even the complex expiratory air from different people.[82] Each pixel unit of this nose array can be designed to show a specific adsorption capacity for a specific vapor gas, leading to different Bragg diffraction shifts and forming a fingerprint mapping to discern volatile analytes. In another work, a monolayer of colloidal

https://doi.org/10.1021/acsnano.1c02495
ACS Nano 2021, 15, 9299−9327

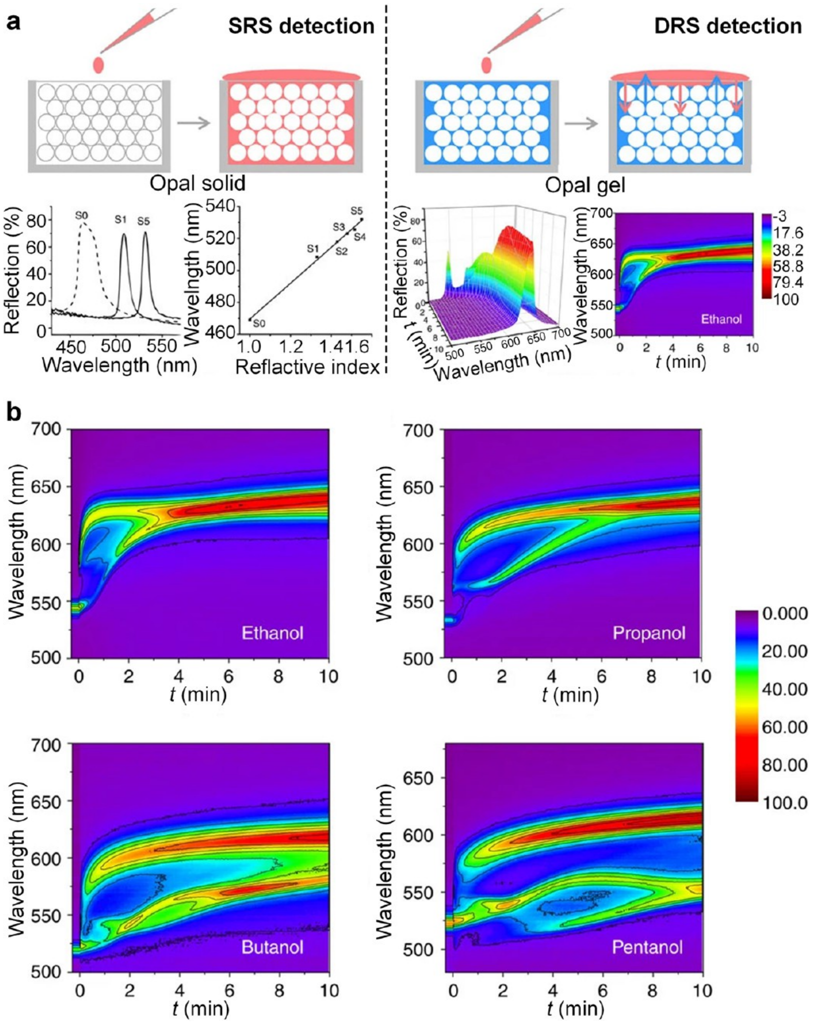

Figure 5. Dynamic sensing of solvents with similar or identical refractive indices using PhC gels. (a) Comparison of PhC gel sensing using SRS and DRS approaches. (b) DRS patterns of homologue alcohols. Reproduced with permission under a Creative Commons license from ref 88. Copyright 2015 Springer Nature.

crystals coated with an ultrathin metal−organic framework (MOF)[46] was reported for highly efficient vapor sensing through the change of the effective refractive index. The sensitivity proved to be strongly determined by the thickness of the MOF coating and thus can be optimized accordingly. Thanks to the enhanced pore accessibility and diffusion efficiency endowed by the MOF layer, a wide dynamic range of the response, ultrafast response rates (<5 s), and excellent recyclability were achieved by this optical motif design. With these advantages, such a design shows a competing alternative technology toward vapor sensing in real time and enables integration with portable devices.

Problematically, we found that for refractive index-induced sensing often a shift of only a few nanometers of the Bragg diffraction is observed, making it difficult to perform accurate measurements by an optical spectrometer. This can bring about issues of reliability and, therefore, an increased refractive index contrast before and after specific binding is highly required. A possible approach to realize this is by tailoring the refractive indices of the constituent materials and the structures of the PhCs. A further problem is that, because the static reflection spectrum (SRS) is a linear function of the refractive index of the detected analyte, it is challenging to differentiate analytes with similar refractive index, for example, homologues, isomers, and solvents with similar structures and physical properties. To address this issue, a method for measuring the dynamic reflection spectra (DRS) of PhC gel[88] was developed, which depends on the interplay of analytes and the PhC gel and are associated with polarity, viscosity, and affinity of the analytes to the PhC gels. We will discuss this method below in section Lattice-Spacing-Induced Sensing.

LATTICE-SPACING-INDUCED SENSING

Mechanically induced changes of lattice spacing or volume of PhC structures can cause a significant shift of the Bragg diffraction peaks according to the Bragg−Snell law. These changes can be caused by changes in charge or osmotic pressure in the PhC in response to analyte binding of such as heavy metals,[89,90] proteins,[53] kinase,[91] and nucleic acids,[38] have been demonstrated. The lattice spacing or volume change generally occurs in hydrogel-based PhC structures with non-close-packed periodicity and is driven by the total free energy of the system. The total free energy of the associated systems includes three different free energies, namely, the free energy of a Donnan-type equilibrium, the free energy caused by elastic restoring forces, and the free energy of mixing.[50,92] A change in

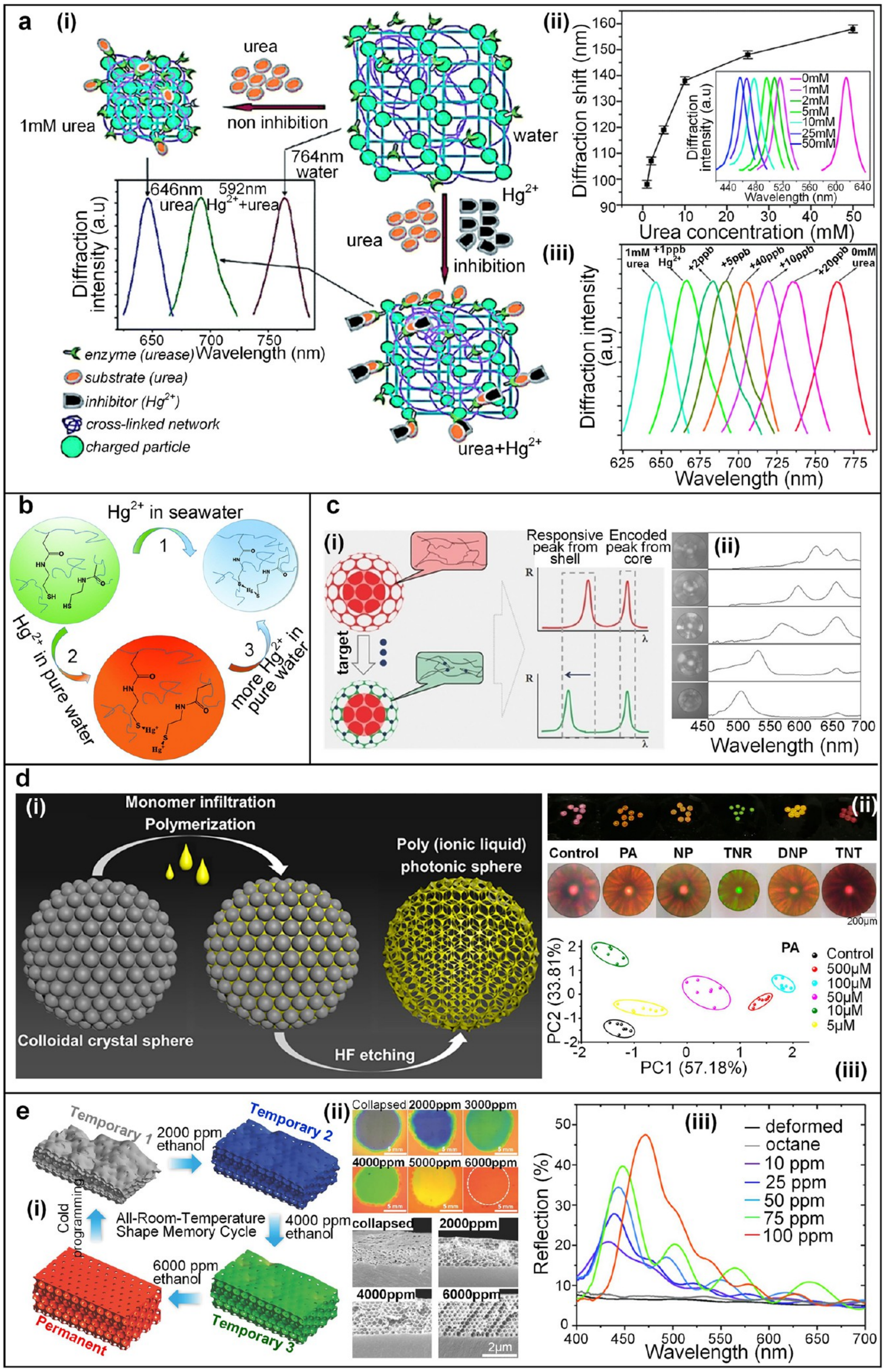

Figure 6. Sensing by lattice spacing variations of PhCs. (a) Urease-immobilized hydrogel opal structures for detection of urea and Hg^{2+}. (i) Diagram of sensing mechanism. (ii) Bragg diffraction peak shifts as a function of urea concentration. (iii) Optical reflection spectra of urease-immobilized hydrogel opals in the copresence of urea and Hg^{2+} with increasing Hg^{2+} concentration. Reproduced with permission from ref 95. Copyright 2011 Royal Society of Chemistry. (b) −SH spatially distributed hydrogel opals for Hg^{2+} sensing through formation of $-S-Hg^{2+}$ and −S−Hg−S− bridges. The formation of −S−Hg−S− bridge bonds in seawater has a blue shift response due to the hydrogel shrinkage, while the formation of $-S-Hg^{2+}$ in pure water has low Hg^{2+} concentration, leading to a swelling with a red shift. Modified with permission from ref 94. Copyright 2017 Royal Society of Chemistry. (c) Core−shell SPCs as a Hg^{2+} sensor. (i) Diagram of sensing principle. (ii) Reflection optical microscopy images and spectra of core−shell SPCs incubated in different concentrations of Hg^{2+}. Reproduced with

Figure 6. continued

permission from ref 96. Copyright 2014 Wiley. (d) Poly(ionic liquid) inverse opal SPCs for visual identification of explosives. (i) Diagram of fabrication procedure. (ii) Photos and optical microscopy images of the SPCs before and after responding to five different explosives at 100 μM. (iii) 2D principle component analysis score plots to evaluate the discriminatory capacity of SPCs in response to different concentrations of picric acid (PA). Reproduced from ref 52. Copyright 2019 American Chemical Society. (e) Shape memory inverse opal structures for analyte detection. (i) Diagram of principle of shape memory inverse opal structures for ethanol analysis. (ii) Photos of the shape memory inverse opal structures (treated by acetonitrile causing structure collapse) and stepwise shape recovery in response to ethanol diffusion from solutions with different concentrations. Cross-sectional SEM images of the collapsed structures and the samples after recovery from ethanol−octane solutions with 2000, 4000, and 6000 ppm ethanol. (iii) Optical reflection spectra of partially recovered samples using ethanol−octane solutions with lower ethanol concentrations. Reproduced with permission from ref 98. Copyright 2018 Wiley.

the total free energy will result in a volume change (swelling/shrinking) of the hydrogel.[50,91,93] For example, in order to differentiate analytes with similar or identical reflective index, a PhC gel consisting of crystalline SiO_2NP lattices and amorphously packed SiO_2NPs was developed by fixing the SiO_2NP patterns dispersed in a mixture of poly(ethylene glycol) methacrylate (PEGMA) and ethylene glycol (EG) (Figure 5a).[88] The DRS of such a sensing material can be continuously recorded once infiltrated with solvents, resulting in a contour map displaying time (as x axis), reflection wavelength (as y axis), and reflection intensity (heat map color). Having a PhC gel containing a solvent (EG) rather than air in solid opals provides benefits, due to the fact that the physical properties of the solvent, namely, polarity, viscosity, refractive index, and affinity, to the PhC gel strongly influence analyte solvent diffusion and polymer deformation, leading to analyte solvent infiltration with lattice expansion or EG extraction with lattice shrinkage. Therefore, the diversified DRS patterns with their specific characteristics can be utilized to discern analyte solvents and even to identify an unknown solvent (Figure 5b).

Another strategy for lattice-spacing-induced sensing is to utilize hydrogel-based PhC structures. The hydrogel-based PhCs can serve as excellent platforms due to the ease of modification by other functional materials (*i.e.*, DNA molecules,[38] carboxylic groups,[89] thiol functional groups,[94] polyelectrolytes,[49] CDs,[90] and enzymes[50]) in order to endow specific recognition capabilities when exposed to the target analytes, resulting in a volume change and optical response. One of examples is the hydrogel suspension array for multiplexed label-free DNA detection that was developed by Gu's group,[38] which integrates both bioresponsive hydrogel SPCs and QD-encoded technology. The DNA-responsive hydrogel SPCs with well-ordered and interconnected porous structures were fabricated by template replication of SiO_2NP lattices combined with acrylamide polymerization and removal of SiO_2NP templates, which can offer high accessibility for target DNA to cross-linked probes of single-stranded DNA (ssDNA). The QD-tagged DNA-responsive hydrogel SPCs can be encoded by incorporating thioglycolic-acid-capped cadmium selenide (CdSe) QDs into the preformed polyacrylamide hydrogel SPCs, and the encoding can be tailored by incorporating different wavelength-emitting QDs into single hydrogel SPC. Furthermore, this QD-tagged DNA-responsive hydrogel SPC has high selectivity and sensitivity with a LoD at the nanomolar level, which is attributed to the specific hybridization of target DNA and the cross-linked and QD-tagged ssDNA in the hydrogel along with a volume decrease. The blue shift of the Bragg diffraction peak on target DNA binding can be used to quantitatively estimate the amount of target DNA.

Also, the Jana group fabricated urease-immobilized hydrogel opal structures for detection of mercury ions (Hg^{2+}) in aqueous media by a change in lattice spacing, accompanied by a Bragg diffraction shift.[95] Figure 6a(i) illustrates the different working mechanisms of these structures for detection of urea and Hg^{2+}. The urease-immobilized hydrogel opals can hydrolyze urea, producing HCO_3^- and NH_4^+ ions inside the hydrogel. These ions then screen the charge of the carboxylate groups of the ionic polyacrylamide backbone (the matrix of hydrogel opals), leading to a shrinkage of the hydrogel with a blue shift of the Bragg diffraction (Figure 6a(ii)). The presence of Hg^{2+} as an inhibitor suppresses the production of ions within the hydrogel and hence the shrinkage (Figure 6a(iii)), resulting in a smaller blue shift compared to the opals that are only exposed to urea. The urease-immobilized hydrogel opals can thus be used both as a urea sensor and a Hg^{2+} sensor with a high selectivity, sensitivity, and reversibility, as demonstrated in their work. The LoD of Hg^{2+} can reach down to 1 $\mu g \cdot L^{-1}$ (1 ppb, ∼5 nM), which is below the maximum contaminant level (2 ppb) suggested by the Environmental Protection Agency, USA, for safe drinking water. Furthermore, Qin *et al.*[94] fabricated PhCs for highly sensitive and selective detection of Hg^{2+} in seawater, namely, −SH-immobilized hydrogel opals with non-close-packed fcc arrays. These −SH-immobilized hydrogel opals can selectively bind with Hg^{2+} ions to form −S−Hg−S− bridge bonds in seawater, causing a shrinkage of the hydrogel. By this design, the resulting Bragg diffraction wavelength shift is proportional to the amount of bound Hg^{2+} ions, enabling the Hg^{2+} ion concentrations with a LoD of 1 nM level in seawater to be quantitatively evaluated. It is worth noting that −SH-immobilized hydrogel opals with different amounts of −SH groups have different specific detection ranges for Hg^{2+} ions, due to the saturation of Hg^{2+} binding to the −SH groups. The authors in addition demonstrated that the LoD for Hg^{2+} ions in pure water (0.1 nM) is different from that in seawater (1 nM), which was attributed to the Hg^{2+}-concentration-dependent ligand formation. At low concentrations of Hg^{2+} in pure water ($<10^{-7}$ M), the single ligand complex $-S-Hg^{2+}$ is formed, and the electrostatic repulsion force between $-S-Hg^{2+}$ complexes leads to hydrogel swelling, while formation of −S−Hg−S− bridge linkages is favored when Hg^{2+} concentration is higher than 10^{-7} M, balancing the repulsive force from $-S-Hg^{2+}$, as shown in Figure 6b.

Hydrogel-based PhCs have, apart from monitoring heavy metal ion concentrations, also been used for monitoring of radioactive metal ions with a LoD of 10 nM for the uranyl ion (UO_2^{2+}). Rich carboxylic-group-functionalized hydrogel opals were used, where a chelation reaction induced a hydrogel shrinkage. This resulted in a blue shift of the structural color which could be distinguished even by the naked eye. These hydrogel opals not only can be used as sensing units for real-

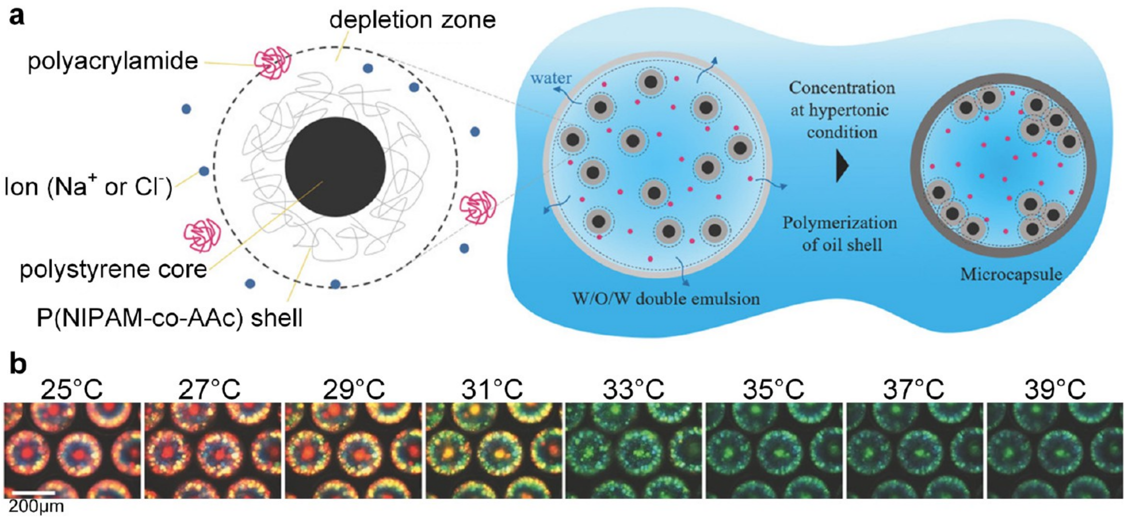

Figure 7. Microcapsule sensor assembled by temperature-responsive core−shell colloids. By observing the color, the temperature can be revealed. (a) Microcapsule sensor fabrication principle by depletion-driven phase separation. (b) Thermochromic properties of microcapsules. Reproduced with permission from ref 55. Copyright 2018 Wiley.

time monitoring of UO_2^{2+} but also can be utilized as adsorbents for purification of wastewater by removal of UO_2^{2+}. A maximum adsorption capacity of 169.67 mmol·kg^{-1} was demonstrated at 298 K.[89]

Additionally, core−shell structure of SPCs with a hcp symmetry have been reported by the Gu group.[96] The structure consists of opal cores as their encoding units and responsive inverse opal hydrogel shells as their probe units. Compared to the QD-tagged inverse opal SPCs as mentioned above,[38] this core−shell SPC integrates the encoding property and decoding ability in one single SPC to achieve Hg^{2+} detection. It can provide stable Bragg diffraction peaks for encoding the cross-linked hydrogels in the capsule shells and achieve target recognition by the corresponding probes, leading to a shrinkage of the shell with a blue shift of the Bragg diffraction. Figure 6c(i) shows the principle of aptamer-based Hg^{2+} detection using these core−shell SPCs. Shells of SPCs cross-linked with a Hg^{2+}-responsive aptamer were constructed for Hg^{2+} detection (Figure 6c,(ii)). These core−shell SPCs show the capability for sensing specific targets without any labels and can be applied for label-free multiplexed assays with the advantages of encoding and decoding in one-step Bragg diffraction peak measurements.

The strategy of dual-mode sensing has also been employed. For example, inverse opal hydrogels infiltrated with CDs have been designed as a dual-mode sensing platform for selective detection of metal ions.[90] This design has the advantage of a simple fabrication procedure without probe molecule pre-immobilization prior to target detection, compared to the above-discussed works. Variation in the lattice spacing of the inverse opal hydrogels induced by metal ions leads to a Bragg diffraction peak shift in the reflection mode and a fluorescence signal change in fluorescence mode. These responses are ascribed to the hydrogel shrinking caused by the strong interaction between the copper ions (Cu^{2+}) and PAA of inverse opal matrix and photobleaching resulting from the CD aggregation once they are exposed to Cu^{2+}, thus achieving dual-mode sensing with a wide linear detection range of 0.1 μM to 7 mM.

Hydrogel-based PhC sensors are generally polymerized non-close-packed colloidal crystals or inverse opal hydrogels,[47,97] where the polymer networks are either covalently functionalized with the probe molecules, or infiltrated with functional nanoparticles (*e.g.*, CDs). Once target analytes diffuse into the functionalized PhC hydrogels, they can react with probes, leading to a change in hydrogel volume and thereby an optical response. Fabrication of these hydrogel-based PhC sensors usually requires multiple steps, including colloidal assembly, hydrogel polymerization, and probe molecule immobilization. The hydrogel used was mostly PAM or PAA, but advances in functional materials have promoted the development of functional polymers as a matrix for construction of PhC sensors, such as poly(ionic liquid), shape-memorable polymers, and liquid crystals.[52,98,99] For instance, Li *et al.*[52] developed inverse opal microspheres composed of urea-functionalized poly(ionic liquid) for visual identification of explosives with a smartphone (Figure 6d). Figure 6d(i) shows the fabrication procedure of these inverse opal microspheres. This design achieves *on-site* detection and discrimination of many explosives and even their mixtures in a real-world context, which is attributed to the strong hydrogen bonding between the urea motifs and the nitro groups of explosives, resulting in different degrees of swelling or shrinking of the microspheres in response to different analytes, accompanied by structural color shifts, as shown in Figure 6d(ii). This shift is bright and obvious enough to be distinguished by the naked eye. The photos in the top row of Figure 6d(ii) were captured by a smartphone, and the bottom row (Figure 6d(ii)) shows optical microscopy images corresponding to the photos in the top row. These microspheres can be applied not only for qualitative analysis of nitroaromatic explosives but also for semiquantitative assays (Figure 6d(iii)). This rational design combines the advantages of improved sensitivity due to the direct capturing and binding of analytes with a high stability of structural colors without interference and photobleaching. It thus shows potential for development of a portable device that can be used at *on-site* locations such as airports, customs, and accident locations. Moreover, smart shape memory polymers have been directly utilized as matrix of inverse opals, as they can memorize and recover their permanent shape in response to an external stimulus, for example, pressure, temperature, light, vapor, and solvent.[100−102] Therefore, they have been

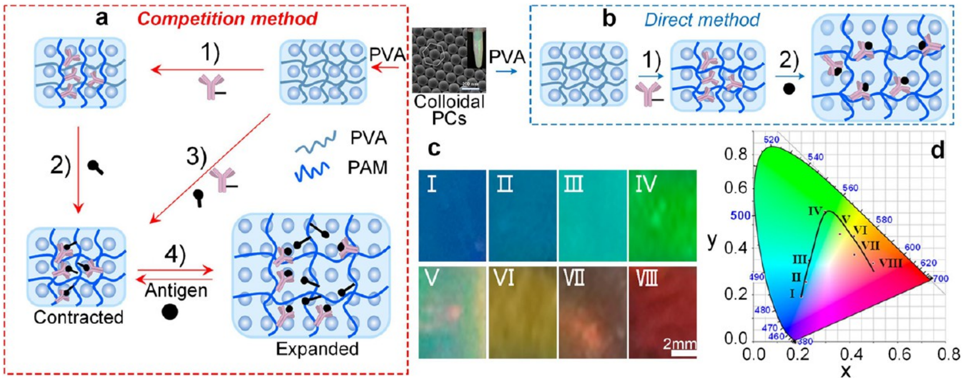

Figure 8. Universal competition-based method for sensing using hydrogel PhCs. (a) Sensing principle using antibody−antigen interaction. Applying transient fixation of well-ordered, non-close-packed PhCs to a poly(vinyl alcohol) (PVA) polymer and covalent immobilization of acrylated antibodies−antigens to a PAM and subsequent PVA removal for fabrication of antibody−antigen grafted hydrogel PhCs. (b) Corresponding direct method for sensing. (c) PrtA sensor (IgG-protein-A-immobilized hydrogel) with obvious color changes in response to different concentrations of antigen. (d) Corresponding CIE (International Commission on Illumination) chromaticity diagram of the PrtA sensor in (c). Reproduced from ref 53. Copyright 2020 American Chemical Society.

extensively exploited for sensing local environment changes induced by the target analytes. Leo *et al.*[98] developed chromogenic inverse opal sensors, using smart shape memory polymers of polyester/polyether-based urethane acrylates blended with tripropylene glycol diacrylate (Figure 6e). The collapsed lattice of inverse opal structures can be recovered stepwise along with a structural color change once exposed to different concentrations of swelling analytes (*e.g.*, ethanol, acetone, and dichloromethane) present in complex, multicomponent nonswelling mixtures (*e.g.*, gasoline and water), as shown in Figure 6e(ii). The photos in Figure 6e(ii) present structural color changes of collapsed shape memory inverse opals and the same sample after recovering from ethanol−octane solutions with different concentrations of ethanol. The corresponding cross-sectional SEM images in Figure 6e(ii) show periodic structures in response to different concentrations of ethanol, indicating a volume increase with increasing ethanol concentration. The authors demonstrated quantitative analysis of ethanol in octane and gasoline with high sensitivity and a low LoD of 10 ppm (0.22 mM), as well as a wide sensing range (Figure 6e(iii)). These inverse opals with shape memory polymers can also achieve ethanol detection in consumer medical and healthcare products. They thus show high potential for applications in environmental monitoring and product control in chemical, petroleum, and pharmaceutical industries. Such designs are inexpensive, reusable, durable, and readily integrated with mobile platforms to create portable sensing devices. Besides the functional polymers serving as matrix of opal structures and inverse opal structures, stimuli-responsive colloids can also be utilized as building blocks for construction of PhC structures for *on-site* monitoring of microenvironmental conditions. For instance, microcapsule PhCs assembled by core−shell colloids have been developed through depletion attraction,[55] where the shell of the colloid is made of temperature-responsive hydrogel (Figure 7a). Figure 7a shows fabrication principle of the microcapsule PhCs (left image) and the crystallization of core−shell colloids at hypertonic conditions (right image). Such a microcapsule sensor, fabricated with high homogeneity and periodic structure by droplet microfluidics, can enable a rapid and broad change of its structural colors in response to changes in temperature while maintaining a close-packed array (Figure 7b).

Zhang *et al.*[99] reported a salicylic acid (Sal)-containing "SiO_2/propylene carbonate" liquid PhC as a photonic sensing material for detection of Cu^{2+} in water. The target analytes containing Cu^{2+} promote the release of H^+ from Sal and result in a shrinkage of the lattice spacing. As a result, the Cu^{2+} concentration can be determined by the blue shift of the reflection of liquid PhCs. This kind of liquid PhC sensor is fabricated in one step without the chemical functionalization of recognition groups, which has the advantages of high repeatability and good reliability when compared to conventional methods.

According to the above discussion, lattice-spacing-induced PhC sensors have been fabricated either by postfunctionalization of a hydrogel matrix or by direct manufacturing using stimulus-sensitive materials as matrix/building blocks. The stimulus-responsive materials are in high demand for the fabrication of PhC sensors due to their improved sensitivity and facile operation for the development of portable, inexpensive, and efficient sensing devices. Additionally, to address the issue of limited Bragg diffraction shifts of hydrogel-based PhC sensors with chemically immobilized probes directly capturing the targets, a competition-based PhC sensing approach has been developed that significantly increases the Bragg diffraction shift such that it can be identified visually by the naked eye. Qin *et al.*[53] reported a competition-based universal PhC biosensor using antibody−antigen interaction (Figure 8), which is capable of robust naked eye detection of various biomolecules (*e.g.*, proteins, peptides, and small molecules) with high sensitivity, selectivity, and reversibility. They have also demonstrated that this sensor design can be extended to fabrication of enzyme-detecting biosensors. Figure 8a,b shows the difference in sensing principle between the competition method and the conventional direct method. In the competition method, competitive displacement occurred in the presence of the analyte (antigen), leading to breaking of the noncovalent "cross-linked" hydrogel and giving rise to a significant but reversible expansion in a manner that depends primarily on antibody recognition. Figure 8c,d demonstrates that this biosensor design features large wavelength shifts upon analyte binding allowing naked eye detection. A concentration as low as 50 $\mu g \cdot mL^{-1}$ (~1.19 μM) of protein A (PrtA) was sufficient to give an obvious color change in the PhC

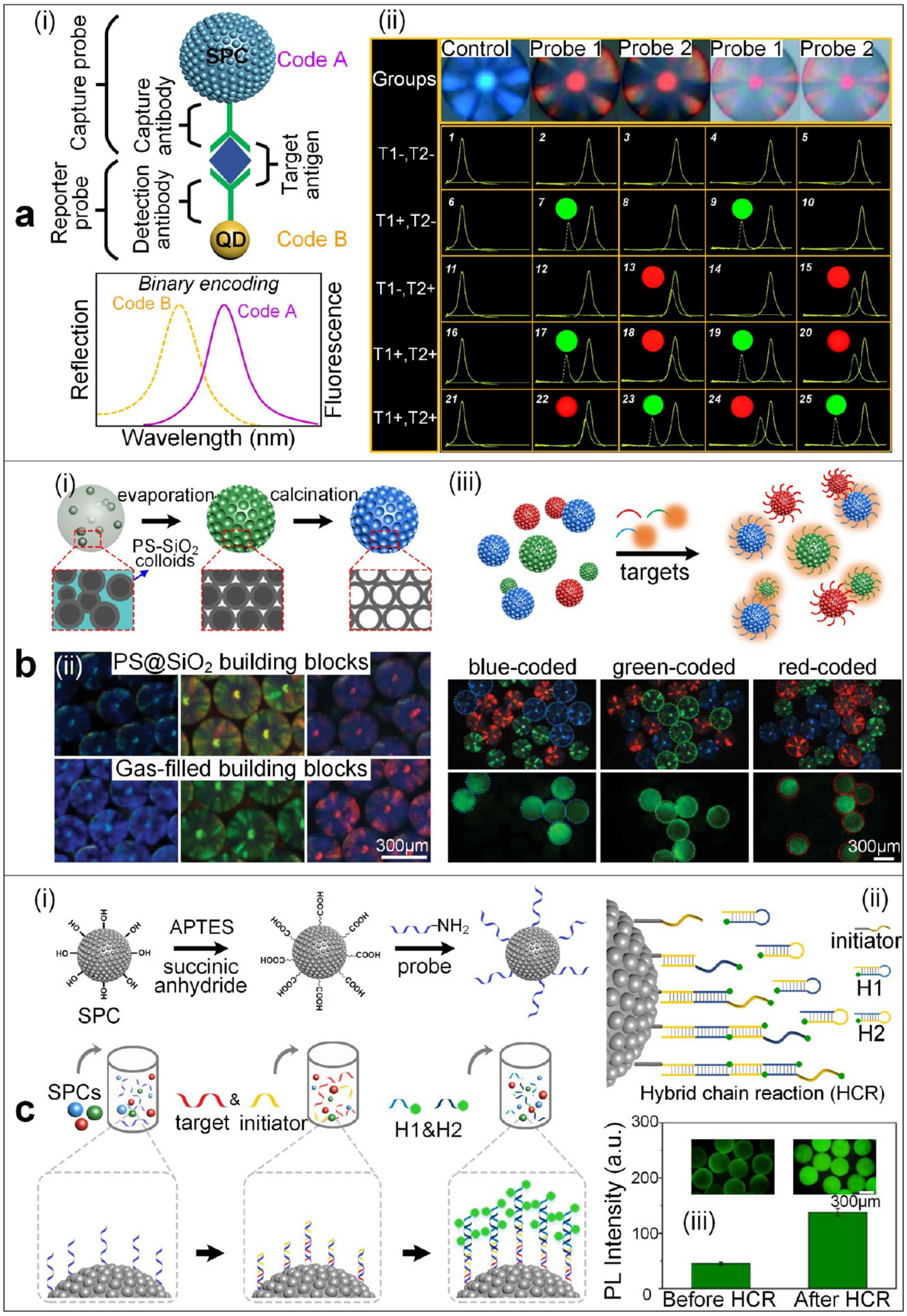

Figure 9. Multiplexed assays by enhanced fluorescence sensing. (a) Binary optical encoding system for multiplex assays. (i) Diagram of binary encoding strategy using SPCs and QDs *via* bridge of antigen−antibody complex (sandwich assay). (ii) Demonstration of multiplexed assays using this binary encoding strategy. The inset solid green and red circles represent the used type of QDs with green and red emission spectra, respectively. Reproduced from ref 119. Copyright 2011 American Chemical Society. (b) Hollow colloidal SPCs assembled from core−shell nanoparticles for miRNA detection. (i) Diagram of fabrication of hollow colloidal SPCs by droplet confinement-induced crystallization. (ii) Optical microscopy images of structural colors of SPCs assembled from solid PS@SiO_2 colloids (top row) and the gas-filled SiO_2NPs (bottom row). (iii) Diagrams of the hollow colloidal SPCs for multiplex miRNA detection and optical microscopy images of three groups of hollow colloidal SPCs after incubation with target miRNA molecules. Top row: bright-field images. Bottom row: corresponding fluorescence images. Reproduced with permission from ref 122. Copyright 2019 Wiley. (c) SPCs combined with a HCR method for detection of bladder cancer miRNAs. (i) Diagram of miRNA detection method using SPCs combined with HCR. (ii) Diagram of the HCR method. (iii) Decoding results of target miRNAs captured by SPCs before and after HCR. Reproduced from ref 109. Copyright 2020 American Chemical Society.

hydrogels, indicating that it is sufficiently sensitive for *in vitro* POC applications.[103,104]

ENHANCED FLUORESCENCE SENSING

As previously reported, fluorescent molecules[105] and nanoparticles (*e.g.*, luminescent semiconductor QDs)[106] have been widely applied in bioassays and diagnosis[106,107] owing to their advantages of encoding and decoding capabilities. However, their sensitivity, selectivity, and efficiency need to be improved because of, for example, the limitations arising from strong interference between barcode units and fluorescence-labeled analytes and photobleaching, as well. Here, PhCs stand out with their capabilities of self-encoding with a much lower fluorescence background and of amplifying optical signal by coupling at the edges of PSBs to emission frequency of immobilized fluorescence materials.[29,108] PhCs have also increasingly gained attention for integration with other methods such as hybridization chain reaction (HCR),[109] FRET,[57] and chelation reaction[110] to increase the sensitivity and lower the LoD. Therefore, we focus on the use of PhCs as both coding units and optical signal amplifiers in combination with fluorescence labels (*e.g.*, fluorophores, QDs, and CDs) for chemical and/or biological sensing with high selectivity and sensitivity.[56,57,110−112]

Molecular recognition groups can be immobilized on as-prepared PhCs to specifically capture analytes such as proteins, DNA, and cancer cells, whereby the analytes are generally labeled with fluorescent groups to deliver a fluorescence signal. Since the encoding capability of PhCs originates from their structural periodicity, they are not subjected to fading, bleaching, quenching, and chemical instability. All of these advantages make PhCs reliable tools for coding. Zhao *et al.*[113] designed SPCs assembled from SiO_2NPs as coding carriers for a multiplex immunoassay. The SPCs with immobilized probe biomolecules provide a larger contact area and more opportunities to capture analytes than the conventional SiO_2 microspheres, which can result in higher sensitivity and lower LoD due to the enhanced fluorescence signal readouts. The use of SPCs as barcodes can eliminate fluorescence interference between target analytes and coding units. In addition, properly designed SPC barcodes can enhance the fluorescence emission intensity, thus enhancing signal readout.[108,114,115] Zheng *et al.*[116] reported aptamer-functionalized SPCs for capture and detection of multiple types of tumor cells in artificial blood samples. The surface of SPCs assembled from SiO_2NPs was decorated with highly branched dendrimer-amplified aptamer probes to capture target tumor cells with high sensitivity, reliability, and specificity. However, the efficiency of cell capture on the surface provided to be strongly influenced by surface topology of the SPCs. Thus, the freshly made SPCs with close-packed nanopatterns were etched to form non-close-packed nanopatterns that were preferred by the cells, leading to improved cell capture efficiency. The probes used are cell-affinitive DNA aptamers, which have high and specific binding affinity to target molecules on the cancer cells; therefore, SPCs with immobilized DNA aptamers can sort multiple types of cancer cells with the advantages of long-term stability, sustained reversible denaturation, nontoxicity, low immunogenicity, and short blood residence time.[117] Moreover, to improve the cell capture efficiency, also inverse opal hydrogel structures with an increased surface area for antibody immobilization were designed to capture and release drug-resistant tumor cells.[118] The antibody-functionalized 3D interconnected porous nanostructures consisting of biocompatible methacrylate gelatin (GelMA) hydrogels are expected to facilitate POC pharmacotherapy and thereby finally improve the patient outcome due to the efficient capture of drug-resistant tumor cells with nearly unchanged viability. The tumor cells can then later be released and used for further studies such as gene detection and drug screening.

In addition, a binary optical encoding strategy for multiplex immunoassays has been developed using the combined optical characteristic spectra of SPCs and QDs.[119] The principle of this binary optical encoding is shown in Figure 9a(i). The antigen can be quantified by the fluorescence signal from the detection of QD-labeled antibodies. Such a design provides both large encoding capacity and high sensitivity with a low level LoD of 58 pg·mL^{-1} (~0.39 pM) and is superior to and more practical than a single SPC or QD encoding. Figure 9a(ii) demonstrates multiplex assays using this sandwich structure of SPCs and QDs according to the dual optical response. The optical microscopy images in the top row (Figure 9a(ii)) are three different SPCs modified with different capture antibodies as capture probes. The left column shows five different groups of analytes. The yellow solid lines and yellow dashed lines indicate the reflection spectra of SPCs and the fluorescence emission spectra of CDs.

Although SPCs have served as excellent barcodes and carriers for suspension arrays,[120] some challenges have to be overcome to further improve sensitivity and LoD of chemical and/or biological assays. SPCs assembled from colloids (*e.g.*, SiO_2NP, PSNP) with a volume fraction of 0.74 and a void fraction of 0.26 have low structural color contrast, especially upon infiltration by surrounding medium due to the further lowered refractive index contrast. As a result, the light transmission is enhanced, leading to a decreased reflection making a decoding process more difficult. Furthermore, due to the high density of composite materials, it is difficult to keep SPCs suspended in reaction solution for a well-developed binding performance.[121] Instead, rapid deposition of the probe-immobilized SPCs reduces the efficiency of the analyte radial diffusion, causing a significant decrease in specific binding efficiency and sensitivity. To overcome these issues, researchers in Zhao's group proposed a SPC, which consists of well-ordered lattices of hollow colloidal nanospheres (core−shell nanospheres) with increased refractive index contrast and high stability in detection solution with a long period of free floating.[122] The hollow colloidal SPCs are also manufactured by a droplet confinement-induced assembly of core−shell colloidal nanoparticles using droplet microfluidics, followed by removal of cores using a high temperature calcination method (Figure 9b(i)). The core−shell colloids used are polystyrene core−silica shell (PS@SiO_2) nanoparticles. The resulting close-packed hollow colloids exhibit an enhanced structural color contrast owing to the increased refractive index contrast which is caused by the gas-filled building blocks (Figure 9b(ii)). The optical microscopy images in the upper row of Figure 9b(ii) show structural colors of SPCs consisting of well-ordered PS@SiO_2 nanoparticles, whereas images in the bottom row show structural colors of the hollow colloidal SPCs with increased color contrast. The authors also successfully demonstrated the use of hollow colloidal SPCs for a multiplexed miRNA assay (Figure 9b(iii)). On the hollow colloidal SPCs functionalized with carboxyl groups with distinct Bragg diffractions, different probes were immobilized for specific binding to fluorescently labeled target miRNA molecules to achieve quantification by characterization of the fluorescence intensity. The hollow colloidal SPCs for multiplexed miRNA assay showed high specificity, low LoD (~100 fM), and anti-interference performance. The LoD is 4 orders of magnitude lower than that of the previously designed SPCs assembled from SiO_2NPs.[113] Additionally, these hollow colloidal SPCs can be integrated with optofluidics for real-time bioassays, which can benefit from both a PSB-enhanced fluorescence signal readout and controllable construction of wettability patterns for enrichment of diluted analytes.[123]

It is still challenging to quantify low-abundance targets, for example, circulating miRNAs in the biological complex matrix of blood. Therefore, amplification strategies (*e.g.*, rolling circle amplification (RCA)[58] or HCR)[124] have been integrated with SPCs for clinical diagnostic applications to improve detection sensitivity.[125,126] For example, SPCs as barcodes were combined with HCR as an amplification method and validated for multiplex analysis of bladder-cancer-related miRNAs (Figure 9c).[109] The probes were decorated on the surface of the SPCs by chemical coupling, and then specific binding of target molecules (miRNAs) with luciferin labels occurred to the SPCs *via* sandwich hybridization. The enzyme-free HCR method is used to amplify the fluorescence signal, not only enabling the LoD for multiple miRNAs in serum to reach 1 nM with high specificity and high throughput but also simplifying the quantification process. Figure 9c(ii) shows the HCR strategy for amplification of the fluorescence signal in detail. Figure 9c(iii) shows the fluorescence image and intensity analysis of target miRNAs captured by SPC barcodes before and after HCR. This design shows potential application in clinical diagnosis and prognostic monitoring strategies for multiplex analysis of bladder-cancer-related miRNAs.

As discussed above, core−shell SPC structures consisting of periodic SiO_2NP lattices as the core (opal structure) and well-ordered interconnected inverse opal porous hydrogel as the shell have been designed for bioassays with the advantages of high coding stability, high binding efficiency, and capability of high density target detection over a wide dynamic range.[58,60] Such a structure has also been employed and integrated with a RCA strategy for multiplex miRNA quantification of low-abundance targets in real-world applications.[58] This design integrates the advantages of both core−shell SPCs and RCA to achieve rapid quantification of low-abundance miRNAs with LoDs at the 10 pM level.

Apart from tailoring the structure of PhCs to improve the detection efficiency and sensitivity, the supporting substrate can offer an alternative way to provide an enrichment functionality for highly diluted samples.[127,128] Droplets with target molecules can be enriched by a wettability difference between the superhydrophilic inverse hydrogel-based SPCs and the superhydrophobic supporting substrate.[127] In this way, a multiplex miRNA analysis with high sensitivity and low LoD at a femtomolar level was achieved.

Compared to the fluorescence label-based HCR method,[109,126] the enzyme-free and label-free methods have raised more attention as they could allow bioassays with low cost and high sensitivity. A strategy was proposed and demonstrated using G-quadruplex-encapsulated SPCs for label-free multiplex detection of mycotoxins with LoD reaching as low as 0.7 pg·mL^{-1} (1 pM).[129] The SPCs serve as a robust encoding carrier, and the decoding process is achieved by G-quadruplex binding with thioflavin (ThT) as an optical fluorescence label (Figure 10). The probes are immobilized on SPCs to form a molecular beacon (MB), which is composed of sequences of mycotoxin aptamers and a G-quadruplex structure. Once the probe-immobilized SPCs have been exposed to both the target and ThT, the hairpin structure of the MB would open due to the specific recognition of aptamer and target, leading to the exposure of the G-quadruplex region. Consequently, a large amount of ThT would bind to the G-quadruplex structure, resulting in a strong fluorescence signal. The mycotoxin concentration is directly proportional to fluorescence intensity of the SPCs, allowing quantitative analysis.

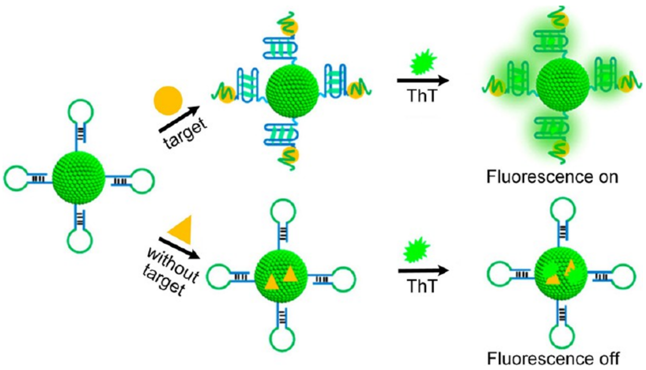

Figure 10. Diagram of label-free quantification of mycotoxins by a G-quadruplex structure and aptamer-immobilized SPCs. Reproduced from ref 129. Copyright 2020 American Chemical Society.

Apart from using probe-immobilized PhCs for bioassays by the enhanced fluorescence spectroscopy, this approach has also been applied for metal ion detection. For example, a 2D PhC dot array on a patterned substrate was developed for sensing of multiple metal ions[130] with high analyte detection performance, using fluorescence signal readouts resulting from analyte-specific quenching enhancement and absorption−emission shifts, which are determined by the electropositivity of various metals.[131] When the edges of the PSBs of PhCs are properly tailored and matched with the characteristic fluorescence peaks, the fluorescence signal readout can be enhanced due to the high DOS of the slow light effect.[114]

The ultimate goal is to employ the PhC barcodes for real-world applications in POC devices in clinical and biomedical areas. One of the examples is development and demonstration of microneedle arrays (MNs) with entrapped SPCs for multiplexed specific analysis of skin interstitial fluid (ISF) biomarkers (Figure 11).[59] Compared to conventional ISF biomarker detection methods using MNs,[132,133] this method has the advantages of (1) facile operation with SPCs entrapped in the MNs without complicated procedures, such as ISF extraction, biomarker purification, and biomarker identification; (2) user friendliness and time efficiency with the assistance of an optical microscope or spectrometer for decoding process; and (3) high biocompatibility, flexibility, sensitivity, versatility, and specificity. The probe-immobilized SPCs on the tip of the flexible microneedle can easily be inserted into the skin and capture specific biomarkers *via* specific biomarker recognition by the probe. The decoding process can be achieved by capturing the corresponding fluorescence probes with formation of sandwich immunocomplexes, where the biomarker concentration can be indirectly quantitatively analyzed by the fluorescence intensity of the SPCs, and the identity of the biomarkers can be determined by

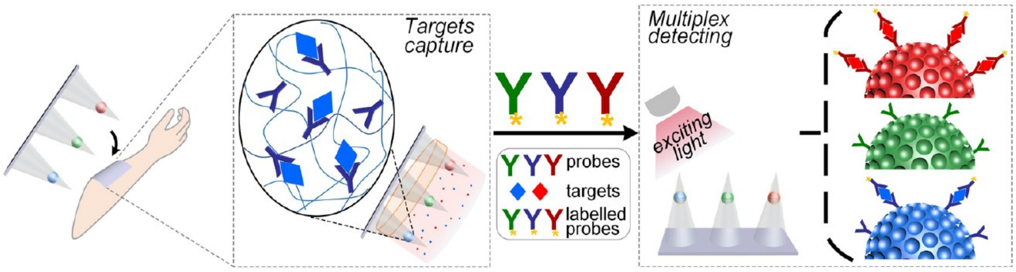

Figure 11. Diagram of microneedles (MNs) encoded with SPCs for ISF biomarker detection. Reproduced with permission from ref 59. Copyright 2019 Wiley.

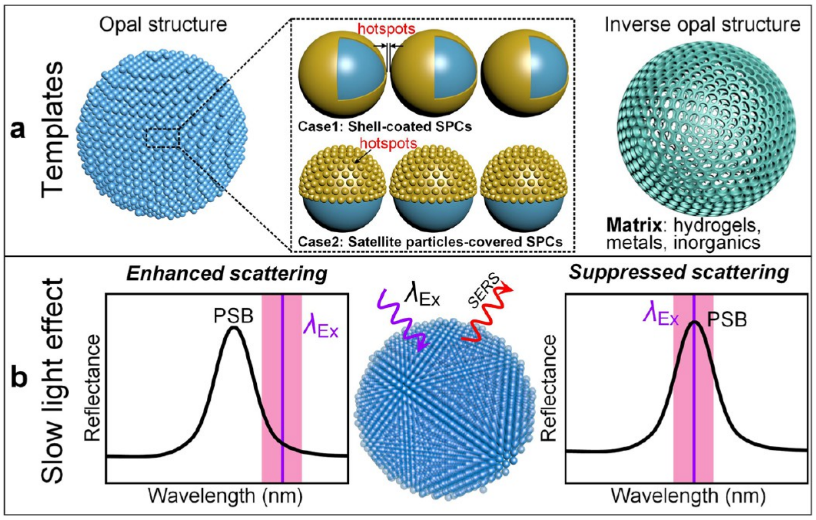

Figure 12. PhCs serving as SERS-active substrates for chemical and/or biological sensing. (a) Diagram of PhC structures as templates for construction of hotspots for SERS. Left side: schematic of opals as templates for fabrication of SERS-active substrates. Right side: inverse opals used for SERS-active substrates, where the matrix can consist of hydrogels, metals, and inorganics. (b) Diagram of light localization and enhancement/suppression of Raman signal by PhCs. Left side: an overlapping of the excitation wavelength (λ_{Ex}) with the red edge of the PSB, which can increase the localized EM field. Right side: light−matter suppression due to an overlapping of λ_{Ex} and the PSB.

the distinct Bragg diffraction peaks of the SPCs. However, there are still many efforts required to develop PhC barcodes for real-world applications in POC devices. For instance, other biomarkers (*e.g.*, proteins, nucleic acids, and ions) need to be investigated and demonstrated. Moreover, the encoding and decoding processes can be integrated by using target-responsive hydrogels as the constituent materials of the SPCs, which can further improve the sensitivity and practicality in clinical diagnostics.

In the above discussions, we found that the LoD and sensitivity can be greatly improved either by precisely tailoring the structure of the PhCs (homogeneous structure, inverse opal hydrogels, opal core−inverse opal shell structure, and decoration of the PhC structure by 2D materials (*e.g.*, graphene))[134] or by integrating with methods to amplify the decoding signal. In addition, the supporting substrate of the PhCs can also be tuned to enrich strongly diluted samples to obtain higher sensitivity and stronger signals. To briefly summarize, PhCs not only serve as encoding units for multiplex assays for proteins, DNA, miRNA, tumor cells, and metal ions but also can be used as an optical signal amplifier to improve the readout signal, improving the sensitivity and lowering the LoD.

SERS-BASED SENSING

SERS has developed into a commonly used noninvasive spectroscopic sensing technique with the advantages of high sensitivity (even near single molecular level), label-free sensing, and small bandwidth of molecular fingerprint, allowing to distinguish molecules with similar structures.[135] Due to well-developed and reliable analytical concept of SERS, SERS-based chemical sensors and/or biosensors have been designed for many different analytes such as single atoms[136,137] (*e.g.*, metal ions), small molecules,[138] biomolecules,[139,140] genes,[141] cells, and tissues.[142,143] The molecules confined at/near nanostructured plasmonic materials[144] can be excited by incident light coupled with the localized surface plasmon resonance (LSPR), resulting from collective oscillation of metal conduction electrons. The most popular approach for amplification of the SERS signal is to construct hotspots where an enhanced localized EM field is produced, as is widely reviewed in the literature.[145,146] A variety of plasmonic nanostructures have been developed to strengthen the localized EM field by tailoring their morphology, dielectric properties, and coupling frequency. Nanostructured plasmonic materials made of metals (*e.g.*, Au, Ag, Cu, and Al)[144,147,148] have been widely explored for SERS enhancement. Besides the contribution of hotspots to SERS signal amplification, PhCs have also long been involved in SERS enhancement as PhCs can aid in concentrating light in space or time with their

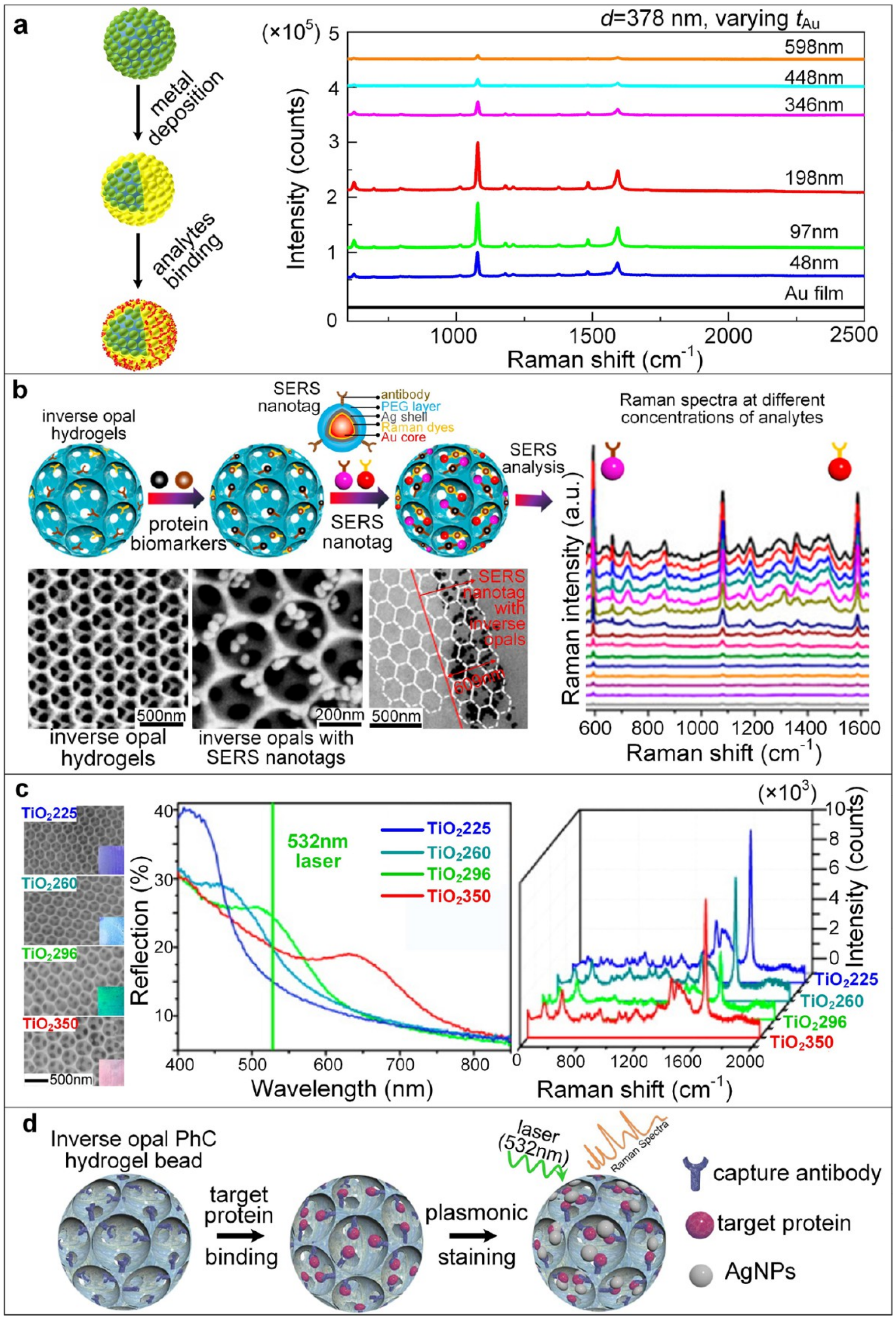

Figure 13. PhC structures used for chemical and/or biological sensing by SERS. (a) Tunable nanogaps between Au-coated SiO_2NPs of SPCs for molecule detection by SERS with an EF of 7 orders of magnitude. Reproduced with permission from ref 150. Copyright 2017 Royal Society of Chemistry. (b) Inverse opal hydrogels with incorporated SERS nanotags (Raman dyes embedded core−shell Au@Ag nanoparticles) for biomarker detection with high sensitivity and a wide dynamic detection range. Reproduced from ref 67. Copyright 2018 American Chemical Society. (c) Plasmon-free inverse TiO_2 PhCs for SERS with improved sensitivity according to the enhanced light−matter interaction. SEM images of inverse TiO_2 PhCs with different size of their building blocks and corresponding reflection spectra, as well as Raman spectra (10^{-5} M methylene blue adsorbed on their structures for detection). Reproduced from ref 64. Copyright 2014 American Chemical Society. (d) Diagram of inverse opal hydrogels featuring AgNPs for multiplexed analysis of proteins by their Raman fingerprints. Reproduced with permission from ref 157. Copyright 2015 Wiley.

periodic photonic structures.[149] Hence, not surprisingly, both PhCs and hybrid materials consisting of photonic−plasmonic structures have been engineered for improvement of the SERS enhancement and have been demonstrated to provide an alternative analytical approach.

PhCs with periodical arrangements can serve as excellent nanostructured templates to load plasmonic materials for construction of high density hotspots as SERS-active substrates with high controllability and reliable repeatability (Figure 12a),[150] but they can also localize excitation light to further enhance the localized EM field owing to the increased DOS. The excitation light located at edges of the PSBs can travel with a reduced group velocity to confine and amplify the localized EM field. Therefore, PhCs as SERS-active substrates for quantification benefit from (1) facile fabrication of high density hotspots with high repeatability and precise controllability,[150] (2) dual tunability of coupling effects with respect to the LSPR properties of plasmonic structures and slow light effect of periodic structures,[151] and (3) controllable physical functionality, namely, superwettability and high adsorption for confinement and enrichment of analytes in liquid state in the proximity of SERS-active substrates, especially important for molecules with a poor or no affinity to the plasmonic surfaces.[152,153]

PhCs can offer well-defined nanostructures as templates for subsequent construction of noble metal nanoslits,[150] clusters,[154] and arrays[4] with high density hotspots for Raman enhancement. For example, by combining methods of droplet microfluidics and metal film deposition, Wang *et al.*[150] reported SPCs covered by metal films featuring a high density of noble metal nanoslits (~20 nm in width) for detection of molecules (even with a small Raman cross section) with an enhancement factor (EF) up to 7 orders of magnitude with high controllability and repeatability (Figure 13a). To further improve target adsorption and binding efficiency and to widen linear detection range, inverse PhC structures have been developed.[63,67] Recently, for example, inverse opal hydrogels were reported for multiplex analysis with the assistance of Raman dye-tagged Au@Ag core−shell colloids.[67] The inverse opal hydrogels with well-ordered and interconnected pores provide substantially increased adsorption efficiency and thus enable a wide linear dynamic detection range, which is of significance for high-throughput screening in diagnostics (Figure 13b). Moreover, multiplex immunoassays on one single inverse opal hydrogel were achieved by bridging the Raman nanotags of Au@Ag core−shell colloids and inverse opals through specific binding, where the decoding can be deciphered by the specific tagged Raman dyes with their characteristic fingerprints. Such a design achieves multiple biomarker immunoassays with high sensitivity and a wide linear dynamic range, spanning over 6 orders of magnitude (10 pg·mL^{-1} to 10 μg·mL^{-1}), and low LoD at 3.6 fg·mL^{-1} (0.05 fM) level for alphafetoprotein (AFP) and 1.9 fg·mL^{-1} (0.01 fM) for carcinoembryonic antigen (CEA). These two biomarkers are normally used as indicators of a series of tumors such as liver and colon tumors for clinical diagnosis. In this proof-of-concept research, PhCs not only provided templates for further finely tailoring the plasmonic nanostructures but also offered an abundance of binding sites due to their large surface-to-volume ratio. A dual-encoding system combining SPCs with gold nanoparticles tagged with Raman dyes for multiple immunoassays has been achieved, as well,[66] where Bragg diffraction peaks and Raman molecule fingerprints can be decoded at once with low background and interference, high stability, and reproducibility. This strategy can well address the demands of high throughput and multiplexed assays.

Additionally, PhCs can couple the Bragg mode with LSPR to improve Raman signal by exploiting slow light effect.[151,155] The coupling of Bragg and plasmonic modes has been well investigated by both purely photonic structures[63] and hybrid structures.[156,157] A plasmon-free TiO$_2$ inverse opal structure[64] has been fabricated for SERS with an improved Raman intensity, where the Raman signal is strongly dependent on the PSB frequency and the excitation laser wavelength (Figure 13c). When the excitation laser wavelength is near the edge of the PSB, an improved Raman signal is obtained that is attributed to the enhanced light−matter interaction by the repeated and multiple light scattering in periodic lattices, whereas when the excitation laser wavelength coincides with the PSB, the light propagation is suppressed with decreased DOS, leading to a decrease in Raman signal. The synergistic effect of photonic and plasmonic enhancement has furthermore been confirmed in hybrid materials.[157,158] Mu *et al.*[157] developed antibody-functionalized inverse opal hydrogels with stained AgNPs for multiplexed analysis of proteins (Figure 13d). This hybrid material benefits from both the inverse opal hydrogels with high binding site densities, and a high density of hotspots, as well as an extra enhancement caused by a coupling of the Bragg and plasmonic modes.

Besides the artificial 3D PhCs fabricated by bottom-up approaches such as confinement-induced assembly,[4] coassembly,[159] and vertical deposition,[160] biological PhCs existing in natural creatures (*e.g.*, butterfly wings and diatom frustules) have also been explored to construct hybrid materials with photonic−plasmonic properties for SERS enhancement, with the advantages of low cost and large-area production.[156,161,162] For instance, 3D sub-micrometer Cu structures replicated from butterfly wings by electroless deposition have been demonstrated for SERS enhancement resulting from periodic rib-structures with high density piled-up hotspots on main ridges (Figure 14a). Diatom frustules have also become increasingly popular due to periodic mesoporous arrays, showing photonic properties and enabling amplification of the SERS signal. Alan X. Wang's group[156] has proposed biological PhC-enhanced plasmonic mesocapsules for achieving single-molecule optofluidic SERS sensing by utilizing biological diatom silica PCs with *in situ* grown AgNPs, as shown in Figure 14b. Not only do diatom silica PhCs serve as carrier microunits for loading high density hotspots produced by the formation of high density AgNPs, but also do submicron pores of the frustules enable an effective analyte capture and mixing inside the microfluidic

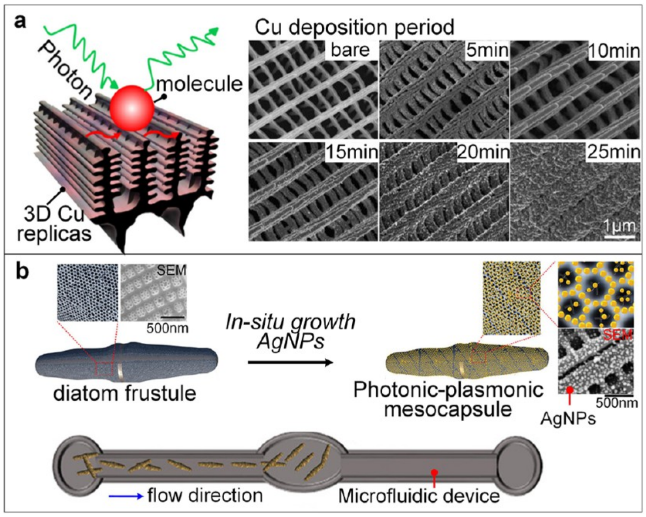

Figure 14. Biological PhCs serving as SERS-active substrates for sensing. (a) 3D Cu PhC structures replicated from butterfly wings by electroless deposition with varying periods (SEM images) for SERS with large-area production and low cost. Reproduced with permission from ref 161. Copyright 2012 Wiley. (b) Diatom PhC-enhanced plasmonic mesocapsules applied for optofluidic-SERS sensing. Reproduced with permission from ref 156. Copyright 2019 Wiley.

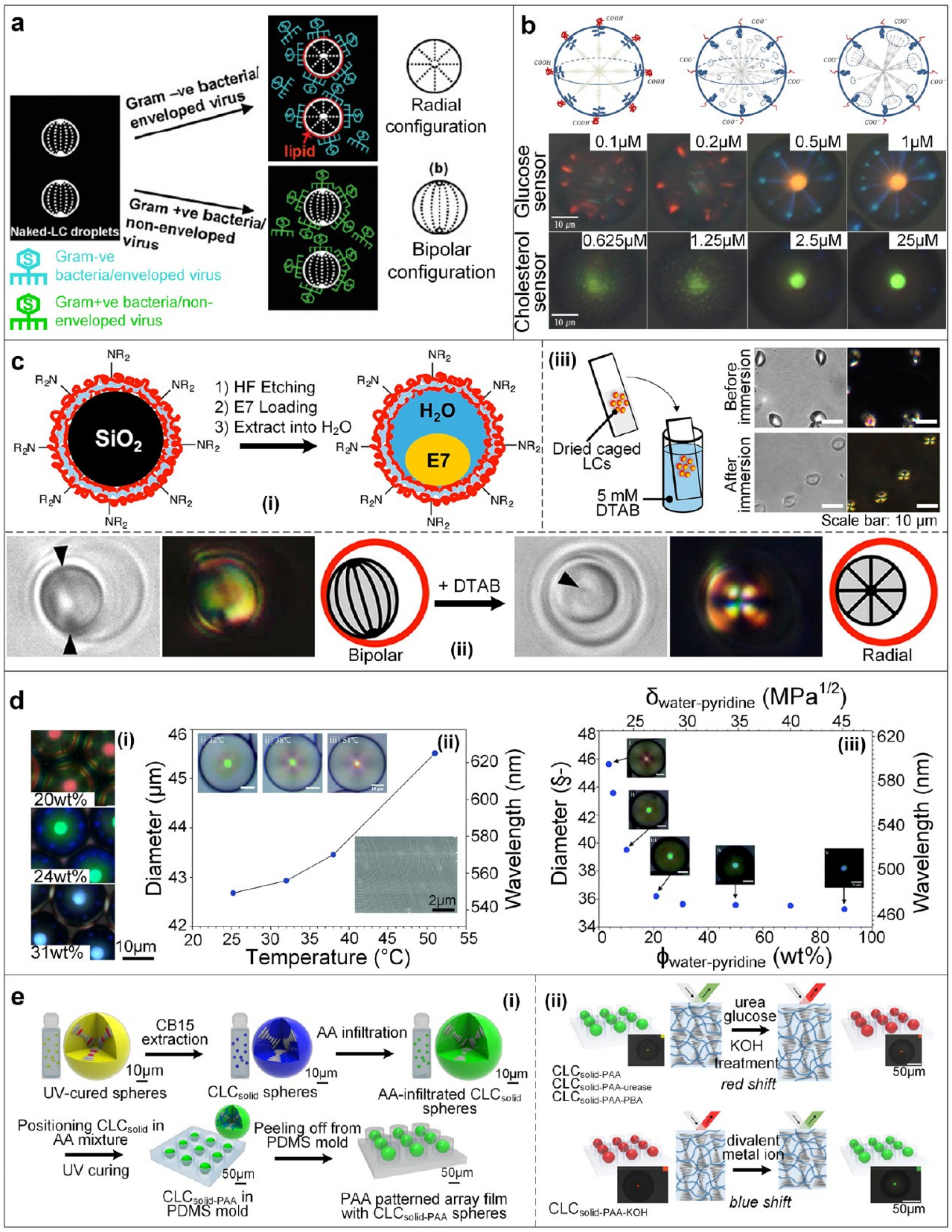

Figure 15. LC-based microdroplets as chemical and/or biological sensors. (a) NLC microdroplet-based virus/bacteria sensor with a bipolar to radial configuration transition. Reproduced with permission from ref 172. Copyright 2009 Wiley. (b) Enzyme-immobilized CLC microdroplets for detection of glucose and cholesterol. Reproduced from ref 183. Copyright 2016 American Chemical Society. (c) Polymer-caged NLC microcapsules with high stability for detection of amphiphiles. (i) Schematic of the polymer-caged NLC microcapsule fabrication procedures. (ii) Bright-field, polarized microscopy images and schematic illustrations of director configuration change of polymer-caged NLC microcapsules in response to the DTAB addition. (iii) Demonstration of LC droplet-based "test strips" consisting of dried caged NLCs that can be dipped into aqueous analyte solution, and the corresponding bright field and polarized microscopy images before insertion and after insertion into a DTAB solution. Reproduced from ref 185. Copyright 2015 American Chemical Society. (d) CLC_{solid} microspheres as solvent quality indicators and temperature sensors owing to the helical pitch change. (i) Optical microscopy of CLC_{solid} microspheres after chiral dopant extraction with red, green, and blue reflection colors at the center, corresponding to the CLC mixtures with increasing concentrations of chiral dopant. (ii) Diameter and calculated wavelength of CLC_{solid} microspheres in toluene as a function of the solvent temperature; insets show optical microscopy images and the cross-sectional SEM image of a CLC_{solid}. (iii) Diameter and calculated wavelength of the CLC_{solid} microspheres as a function of water content in a pyridine/water mixture at 24.0 °C; insets show the corresponding optical microscopy images. Reproduced with permission from ref 75. Copyright 2017 Royal Society of Chemistry. (e) Multisensor platform made of a PAA-interpenetrated CLC_{solid} microsphere ($CLC_{solid\text{-}PAA}$) patterned film. (i) Schematic of preparation of photonic $CLC_{solid\text{-}PAA}$ microspheres in a patterned array film. (ii) Multianalyte sensing using the receptor-immobilized photonic $CLC_{solid\text{-}PAA}$ microspheres. Reproduced from ref 69. Copyright 2020 American Chemical Society.

channels. In addition, this diatom frustules can enhance the local EM field through photonic crystal effect of guided-mode resonance[163] in the visible wavelength range. These reported hybrid materials achieve single molecule detection of R6G in microfluidic devices and showed a higher analytical enhancement performance than PhC cavity-trapped AgNPs integrated in a microfluidic chip.[164] Furthermore, detection of benzene and chlorobenzene compounds in tap water with near real-time response and a LoD reaching 1 nM has been realized.

CONFIGURATION TRANSITION-INDUCED SENSING

LC materials have been widely applied in bioassays, displays, and optoelectronic devices owing to their physical and optical properties.[165,166] LCs can organize into well-defined structures with collective physical and optical properties. Their well-oriented physical configurations can be easily discerned by a polarized optical microscope and the selective Bragg reflection by an optical spectrometer.[73,166] In addition, the physical configuration and selective Bragg reflection are both sensitive to changes in external environment and to stimuli, accompanied by a response to such substances as heavy metals,[68,167] surfactants,[168] biomolecules,[166,169,170] lipids,[171] bacteria,[172] mammalian cells,[173] gases[174] and light,[175] electric field,[165] and so on. Therefore, in the stimulus-responsive scheme, they can serve as transducers with amplified signal readout in terms of changes in configuration and selective Bragg reflection. The director field ($\boldsymbol{n}$) configuration of LCs is determined by the balance between elasticity and interface anchoring energy and can thus be disrupted or self-reorganize by an adsorption or reaction of chemical and biological substances occurring on the LC−aqueous interface.[176] Consequently, a change of the director field configuration can be applied for sensing. Furthermore, a nematic LC (NLC) host doped with a chiral dopant can form into another kind of soft-state PhC with helical organization of mesogenic molecules, which are termed cholesteric liquid crystals (CLCs). The CLC shows a selective PSB, which is determined by the helical twisting power (HTP) and is tuned by molar concentration of chiral dopants (c) mixed in NLC and external stimuli. We can regard CLCs as a series of particular NLC layers with a full rotation along the helical axis in a single period of helical pitch. As a result, they can be used as sensors, due to a change in PSB caused by the pitch variation.[177] The selective PSB can be expressed by $\lambda = np$ and $p = 1/(c \times \mathrm{HTP})$. Here, λ is the wavelength of selective reflection (PSB), n is the averaged refractive index of the CLCs, and p is the helical pitch, which can be tuned by external stimuli such as temperature, light, humidity, and ionic strength.[178−181] Value of p also correlates with the molar concentration of dopants (c) and the HTP of dopants.

Here, we elaborate on the use of LC droplets for chemical and/or biological sensing. They have the merits of a large surface area and fast equilibration of analytes with LC droplet interfaces compared to 2D planar interfaces and furthermore of a manufacture that is straightforward and low cost.[182] Also, droplet-based LC sensors enable localization and concentration of specific targets from a diluted medium by surface functionalization. For example, NLC emulsions were developed to sense and differentiate Gram-negative bacterial *E. coli* and the enveloped virus *A/NWS/Tokyo/67* in water.[172] Exposure of the emulsion surface to lipids thereby enabled the reorientation of their ordering (Figure 15a). The monodispersed NLC emulsions were replicated from mesoporous SiO_2 microparticles coated with multilayer polyelectrolytes using a layer-by-layer (LBL) approach. The LoD of this microdroplet-based NLC sensor reached values as low as 10^4 pfu·mL^{-1} of the virus. The LC droplet surfaces can also be functionalized with reactive species for detection of a wide range of analytes with a fast response by a configuration transition. Poly(acrylic acid-*b*-4-cyanobiphenyl-4-oxyundecylacrylate) (PAA-*b*-LCP)-coated 4-cyano-4-pentylbiphenyl (5CB) microdroplets have been reported for glucose detection,[182] where the glucose oxidase (GO_x) is immobilized on the PAA chains. A radial to bipolar configuration change can be observed when the functional 5CB droplets are exposed to glucose. The functionalized 5CB droplets can detect glucose at concentrations as low as 30 μM with a fast response in ∼3 min and high selectivity. The authors furthermore designed a PAA-functionalized CLC droplet (denoted CLC_{PAA})[183] for detection of glucose and cholesterol with a LoD of 0.5 and 2.5 μM, respectively, and a fast response within ∼4 s. The response can be readily distinguished using a normal optical microscope by the configuration transition from a chicken-skin-like pattern to a central dot pattern (Figure 15b). A polarization microscope is thus not needed. Possibly, the configuration change is caused by a local pH change as the enzyme-catalyzed reaction induces a decrease in pH. On the other hand, the configuration change might also be attributed to the specific binding, which can lead to the conformational disruption of the immobilized PAA chains. The CLC droplets are made of nematic host MLC-2132 (Merck, U.K., nematic to isotropic transition temperature: 114.0 °C) and shape-persistent chiral dopant (*S*)-4-cyano-4′-(2-methylbutyl)-biphenyl (CB15). The schematic diagram in Figure 15b shows CLC configuration changes at low pH with a central spot pattern, and at high pH with either a chicken-skin-like pattern or a flashlight pattern. The optical microscopy images in bright-field illumination (Figure 15b) demonstrate how CLC_{PAA} composed of 35 wt % chiral dopant (denoted $CLC_{PAA\text{-}GOx}$) with immobilized GO_x for glucose sensing shows different configurations with varying glucose concentration. Also, $CLC_{PAA\text{-}ChO}$ droplets composed of 40 wt % chiral dopant (denoted $CLC_{PAA\text{-}ChO}$) with immobilized cholesterol oxidase (ChO) show a clear pattern transition with increasing cholesterol concentration.

NLC microdroplets coated with poly(L-lysine) (PLL) by a LBL assembly method have been reported for cell-based sensors.[184] These PLL-coated NLC microdroplets show the capability of adhering to cells with high biocompatibility, accompanied by a radial to bipolar configuration transition. Additionally, the NLC droplets that are attached to cells can detect the presence of toxic agents in the cellular environment and monitor biological interactions, for example, Annexin V−phosphatidylserine binding. As the freely floating bare LC droplets create issues of easy coalescence, fast precipitation, poor stability, and cross-contamination by the nontargeting analytes, polymer-caged NLC capsules (Figure 15c) were developed as biosensors with a high stability, which is even reversible upon rehydration.[185] The fabrication of these polymer-caged NLC capsules is shown in Figure 15c(i), combining procedures of LBL assembly of polyelectrolytes, removal of SiO_2NPs, NLC loading, and deionized water extraction. The authors demonstrated amphiphile sensors that, for example, responded to dodecyltrimethylammonium bromide (DTAB) with a bipolar to radial configuration transition (Figure 15c(ii)). These polymer-caged NLC capsules can be stored for several months without losing the ability to respond to the presence of analytes upon rehydration (Figure 15c(iii)).

It is well-known that liquid microdroplets are of particular interest as whispering gallery cavities (WGC) with the merits of perfect geometry, smooth surface, and high flexibility.[186]

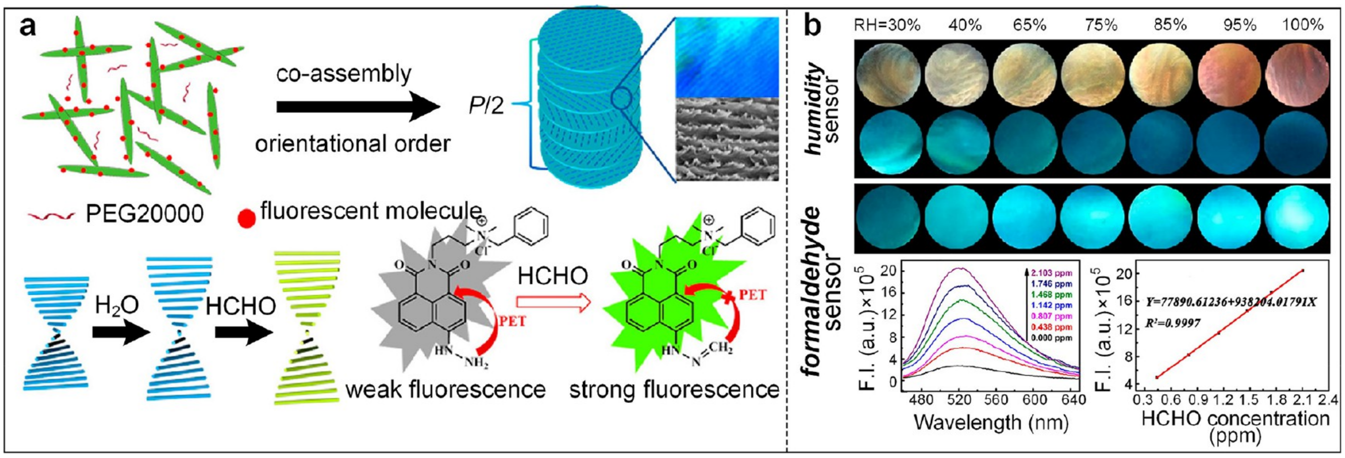

Figure 16. Fluorescent chiral PhC film used for multianalyte sensing. (a) Schematic of a straightforward coassembly process for fabrication of the fluorescent PhC film and the sensing mechanism to water and formaldehyde. (b) Optical responses of the PhC film to RH and formaldehyde. Humidity sensor: Photographs of films upon irradiating with white light (top row) and 365 nm UV (bottom row). Formaldehyde sensor: Photographs of the film upon UV radiation with 365 nm (top row from left to right with increasing formaldehyde concentration). The corresponding fluorescence spectra and the fluorescence intensity as a function of formaldehyde concentration at RH = 65% (bottom row). Reproduced from ref 74. Copyright 2020 American Chemical Society.

The propagation of light waves in the microdroplet is concentrated near the interface, where the field is resonantly amplified by constructive interference. LC-based microdroplets have been investigated as temperature sensors due to their capability of large thermal response and ultrahigh quality (*Q*) factors (near 1000)[187] resulting from the thermo-optic effect, a perfectly spherical geometry and extremely smooth surface. For instance, Zhao *et al.* developed tunable whispering gallery mode (WGM) resonators using dye-doped CLC microdroplets and demonstrated their application as temperature sensor with a maximum temperature sensitivity of up to 0.96 nm·$°C^{-1}$.[187]

In order to further improve stability of liquid-state LC-based sensors, stable solid-state LC sensors have been proposed.[75,188] Park's group[75] designed a solid-state CLC microsphere (CLC_{solid}) (Figure 15d) composed of a reactive nematic LC mesogen mixture and a nonreactive chiral dopant using droplet microfluidics followed by photocuring and chiral dopant extraction without losing the quality of the helical photonic structure and with well-preserved selective Bragg reflection. The helical pitch can respond to external stimuli with a reversible reflection color change due to the refractive index change of the occupied dopant space, which is strongly influenced by the solvent quality, temperature and humidity. Such a CLC_{solid} microsphere can therefore be applied as a temperature sensor and indicator of solvent quality and humidity. Figure 15d(i) shows the CLC_{solid} microspheres with different selective Bragg reflections, which are tuned by the amount of the constituent chiral dopant. The reflected color shows a red shift with an increase in helical pitch in response to an increased temperature (Figure 15d (ii)). The inset SEM shows cross-sectional view of a dried CLC_{solid} microsphere structure after dopant extraction. A solvent sensor is presented in Figure 15d(iii). When CLC_{solid} microspheres are exposed to a mixture of pyridine (as a good solvent) and water (as a poor solvent), an increase in water content results in a blue shift of Bragg reflection to the initial state. Recently, Park *et al.* reported a multisensor platform[69,189] which integrates an interpenetrating polymer network (IPN) within CLC_{solid} microspheres. A patterned film is obtained with capabilities of multianalyte detection *via* prior immobilization of probes or receptors on the IPN network. The detailed fabrication procedure for such polymer-interpenetrated CLC_{solid} microspheres is shown in Figure 15e(i). This platform, with capabilities of the naked eye detection, combines the advantages of the stimulus-induced volume change of a penetrated smart hydrogel network for specific recognition with the reflected structural color of CLC_{solid} microspheres as a signal transducer. To this end, the remaining spaces after dopant extraction can be refilled with a smart hydrogel network such as PAA, which is a weakly anionic polyelectrolyte with a charge state that closely depends on the pH of the system. Since biological systems can induce pH changes, they could demonstrate pH-responsive biosensing as well as pH changes associated with the detection of divalent metal ions, urea and glucose, using specific immobilized receptors (Figure 15e(ii)). For the detection of urea and glucose, the response is attributed to the change of pH resulting from the analyte−probe interaction, whereas the identification of divalent metal ions is attributed to the bridging of the carboxyl groups forming −COO−M−COO− (M: divalent metal ions), causing deswelling of $CLC_{solid\text{-}KOH}$. The high selectivity and diagnostically relevant LoD of the system can be applied for multiple clinical diagnosis by various combinations of smart hydrogel networks and receptors.

Additionally, Schenning's group developed a self-reporting optical calcium sensor using a CLC polymer loaded with preorganized (benzoate) binding sites. External stimuli caused an helical pitch change along with a change in selective Bragg diffraction.[48] The specific binding between Ca^{2+} and benzoate can give raise to a large decrease in the length of helical pitch with a blue shift due to the polymer shrinkage resulting from film dehydration.[190] Therefore, this CLC film can be used as an alternative readout system for an important diagnostic parameter of the amount of total calcium (between 2.1×10^{-3} and 2.6×10^{-3} M) in blood of a healthy human since the selective Bragg reflection shifts occur in a wide concentration range of 10^{-4} to 10^{-2} M Ca^{2+}, which coincides with the range of calcium in human blood.

Also, CNCs normally derived from various natural cellulose sources by acid-catalyzed hydrolysis,[191] have been investigated for assembly into chiral nematic PhCs[192] on water evaporation from a CNC suspension of appropriate concentration. Co-assembly of CNCs with functional molecules such as functional ionic compounds,[193,194] polymers[195] and fluorescent molecules,[74] can regulate the change of texture and pitch of the chiral nematic PhCs in response to external stimuli. The resulting system can then perform chemical or biological sensing with good selectivity and sensitivity. A flexible free-standing CNC PhC film[194] has been developed through coassembly of CNCs and citric acid (CA) owing to the plasticizing effect of CA. Such PhC films can show structural color changes upon external stimuli, including ethanol, alkali, and volatile chemicals. Upon ethanol diffusion into such a PhC film, the structural color shows a red shift due to the increased helical pitch of the chiral nematic CNCs due to the high solubility of CA in ethanol. In addition, when the PhC film is exposed to alkalic compounds such as the mixture of pyridine-ether solutions as demonstrated by the authors, the structural color shows a blue shift. This blue shift is attributed to the neutralization reaction between the −COOH− group of CA and the $-NH^+$ group of pyridine, causing a weakened electrostatic repulsion between CNC and CA and hence a decrease in pitch. All of these externally induced structural color changes can be distinguished by the naked eye with great potential for chemical sensing and environment monitoring. Furthermore, in order to identify trace amount of analytes, the group of Gao has reported a chiral nematic PhC film containing fluorescent molecules, which can form an extremely sensitive off-on fluorescence switch in response to trace amounts of formaldehyde (HCHO) at the molecular level, such as present under indoor atmospheric conditions.[74] By the evaporation-induced coassembly of PEG and a fluorescent naphthalimide derivative containing a cationic group on the CNC surface, the assembled PhC film can respond to multiple surrounding molecules (Figure 16a). Figure 16b shows the responses of the PhC film to humidity and trace amounts of formaldehyde. Particularly, a very strong linear relationship exists between the fluorescence intensity and the formaldehyde concentration at 65% relative humidity (RH), indicating the capabilities of quantitative determination of ultralow levels of formaldehyde in humid conditions. The sensitive off−on fluorescence response to formaldehyde results from the generation of an electron-deficient group ($-N{=}CH_2$) that blocks the photoinduced electron transfer in the fluorescent group and also prevents aggregation of the fluorescent molecules by $\pi-\pi$ stacking.

Even though integration of molecules with CNCs for assembly of smart PhC films for various sensing purposes has been widely exploited, there are rare reports of coassembly of CNCs with functional colloids[196,197] such as plasmonic materials, for the formation of dual/multifunctional PhC films for use in bioassays. One example of a chiral plasmonic film formed by coassembly of CNCs with gold nanorods was given by Querejeta-Fernández *et al.*,[196] demonstrating plasmonic chiroptical properties. Notwithstanding a need for chiral molecular sensing,[198,199] the use of such a hybrid PhC film as a sensor has not been well exploited.

SUMMARY AND OUTLOOK

We have reviewed the literature on self-assembled PhCs as label-free chemical and/or biological sensors, discussing and comparing their relevant structural design, constituent materials and sensing principles. These structure-related properties of the PhCs are highly advantageous for constructing label-free chemical or biological sensors with high selectivity and sensitivity and low LoD. When PhCs are used for quantitative or semiquantitative chemical or biological sensing, five sensing principles can be distinguished based on refractive index change, lattice spacing change, enhanced fluorescence, SERS, and configuration transition. Refractive index changes, lattice spacing-induced Bragg peak shifts and/or structural color changes serve as indicators upon external stimuli. Hereby an enhanced refractive index contrast and a large change of spacing are desired as reaction to the stimulus. Enhanced fluorescence spectroscopy and SERS-based sensing employ the increased DOS in PhCs, causing an amplified electromagnetic field and enhanced light−matter interaction. Configuration transition-induced sensing is of particular interest in 1D PhCs made of NLCs and CNCs, in which a clear response in molecular arrangement and the resulting pitch is required.

In these regards, great efforts have been devoted to engineering finely tailored structures including opal and inverse opal structures, consisting of a matrix of hydrogels, functional polymers, metals or semiconductors and solid colloids or air voids, hybrid core (opal)−shell (inverse opal) structures, hollow structures, and helical structures by helicoids with augmented physical and optical properties. From the point of structural design, these delicate structures were developed to boost both physical and optical properties such the PSB, slow light, and LSPR. Inverse opals are superior to opals owing to the enlarged surface area increasing analyte adsorption and an enhanced refractive index contrast causing improved sensitivity, which is of particular interest for refractive index-based sensing. The hybrid core−shell and hollow structures made of hollow colloids combine both the strength of opals and inverse opals. They are capable of stable coding for multiplexed label-free assays and also enhancing analyte adsorption and refractive index contrast. In addition, the control of the wettability of PhC films by surface compartmentalized functionalization has been investigated for analyte enrichment and with the purpose of microfluidic integration for *on-site* and *in situ* detection. Helical photonic structures show great potential for chiral molecular sensing owing to their chiroptical properties though only a few works have been reported so far. Though numerous PhC structures made of spherical colloids have been applied for sensing, there is still a great potential for the investigation of PhCs assembled from nonspherical colloids. Most of the sensing platforms using assembled CNCs are based on chiral photonic films. The performance of droplet-confinement assembled CNCs in sensing applications is unknown.

The constituent materials of the structures mentioned above form a critical factor for realizing an efficient sensing platform. For refractive index-based sensing, the use of the static reflection spectrum to distinguish chemicals with similar refractive index, or of the same family of chemicals is a great challenge. A way to overcome this limit is to employ a dynamic monitoring approach. Time-dependent Bragg peak mapping can differentiate chemicals with similar or the same refractive index owing to the specific interplay of the constituent material of PhCs with the analytes. This makes the development of materials that are “smart” due to their tailored interactions with the analyte essential for an efficient refractive index sensor. Lattice spacing-based sensing results from volume swelling/shrinking in response to analytes, and often occurs in soft materials and especially in hydrogels, either hydrogel matrices or hydrogel colloids. The use of hydrogels enables versatile functionalization through covalent or noncovalent bonding to realize high specificity. The use of functional polymers as filling matrix or the use of functional nanobuilding blocks can also result in the construction of smart PhCs with straightforward operation and high sensitivity. Considering SERS-based sensing, in order to increase the near field enhancement or hotspots, plasmonic nanomaterials have been integrated into PhC structures, leading to the coupling effect of the photonic mode and LSPR. Additionally, owing to their periodic arrangement, PhCs can serve as templates to guide the distribution of the incorporated plasmonic materials, causing them to be well distributed on surfaces or inside PhCs. In the configuration transition-based sensing platform, addition of or functionalization with other functional molecules, polymers or colloids to the LC host system can result in a high selectivity and sensitivity to target analytes. Also, the coassembly of guest functional materials with the host materials can give rise to chiroptical properties for chiral molecular detection.

With well-tailored PhCs, quantitative or semiquantitative sensing has been realized of a variety of analytes, including ions, small molecules, biomolecules (nucleic acids, proteins, biomarkers), bacteria, and cells, as well as chemicals in vapor, humidity, and temperature, leveraging the optical response of PhCs in the visible spectral region. Fundamental studies indicate the possibility for surface-enhanced infrared spectroscopy-based sensing by tuning the size of building blocks to shift the optical response to the mid-infrared spectral region. In this case the molecular vibrational fingerprint will be highly useful for dynamic process monitoring. Furthermore, there is a shortage of chiral molecular sensing,[200,201] especially using hybrid photonic films with chiroptical plasmonic properties.

Although significant advances in self-assembled PhCs as chemical and/or biological sensors have been achieved, there remains some challenges to be overcome for real-world applications.

(1) *Sensitivity*. Sensitivity is defined as the change/shift in the measured signal per unit of target analyte. A high sensitivity is required for an efficient sensor, as it would enable detection by without the use of a spectrometer or even the naked eye. Such a sensor will be suited for integration into a compact miniaturized chip. Toward this end, the refractive index contrast of the constituent materials of a PhC can be further improved by assembly of hybrid core−shell colloids or by integration of plasmonic nanomaterials. A competitive method or a sandwich immobilization approach on PhCs can be used to increase the change of lattice spacing, causing a larger spectral shift and color change. Moreover, an off-on colorimetric sensing approach can be designed either by integration of fluorescent molecules/particles with host PhCs, or by using a narrow-band light source for illumination. To improve the sensitivity of the sensing platforms that are based on enhanced spectroscopy, structures with amplified near fields and an increased DOS are needed, which can be engineered at low cost by carefully tailoring the coupling between the PSB and the excitation frequency *via* appropriate material selection and structure engineering.

(2) *Selectivity*. For the lattice spacing, enhanced fluorescence and configuration transition-based sensing, preimmobilization of the probes on the PhCs can achieve a high specificity for target analyte binding. It can be expected that SERS-based sensing will become complex by the strategy of probe immobilization, as the added signal complexity due to the biomolecular binding component makes it even more difficult to distinguish the characteristic Raman peaks of the target. SERS nanotags can be integrated into either probes or targets to realize specificity for a wide range of complex biological compositions. However, it will still be challenging to monitor dynamic processes in biological system *via* this nanotag.

(3) *Integration into portable devices*. The sensing principles of enhanced fluorescence spectroscopy and SERS can provide assays with high selectivity, sensitivity and low LoD. However, complex instruments are required to measure the optical signal, which complicates attempts to integrate these methods in a portable device. This makes the exploitation of spectrometer-less sensing techniques increasingly relevant. LCs serving as sensors combine the advantages of easy operation and fast response, but the LoD is relatively higher compared to other sensing principles. Possibly, an increase in analyte surface coverage and a surface functionalization for high specificity may enable obtaining lower LoDs. We expect that the development of advanced materials and of well-tailored structures, combined with integration with smart instruments such as the mobile phone and the use of artificial intelligence (AI) techniques can facilitate the portable sensing.

(4) *Analytes in bodily fluids*. Another major challenge that needs to be overcome for every medical POC device is the complex composition of bodily fluids, which is the cause of the hitherto limited demonstration of direct detection of biomarkers and ions in bodily fluids in literature. This complex composition reduces the sensitivity, and necessitates a large selectivity as many target analytes in bodily fluids occur only in trace amounts and hence are subjected to interference from other substances without purification. Thus, improving the specificity and lowering the LoD remains of critical significance for POC devices. Further tailoring PhC structures and seeking smart materials, and integrating the Lab-on-a-Chip functionalities of sample pretreatment, analyte enrichment might help achieve this in the future.

AUTHOR INFORMATION

Corresponding Author

Juan Wang − *BIOS Lab on a Chip Group, MESA+ Institute for Nanotechnology, Technical Medical Centre & Max Planck Center for Complex Fluid Dynamics, University of Twente, 7522 NB Enschede, The Netherlands;* orcid.org/0000-0002-7334-1733; Email: juan.wang@utwente.nl

Authors

Pepijn W. H. Pinkse − *Complex Photonic Systems Group, MESA+ Institute for Nanotechnology, University of Twente, 7522 NB Enschede, The Netherlands*

Loes I. Segerink − *BIOS Lab on a Chip Group, MESA+ Institute for Nanotechnology, Technical Medical Centre & Max Planck Center for Complex Fluid Dynamics, University of Twente, 7522 NB Enschede, The Netherlands*

Jan C. T. Eijkel − *BIOS Lab on a Chip Group, MESA+ Institute for Nanotechnology, Technical Medical Centre & Max Planck Center for Complex Fluid Dynamics, University of Twente, 7522 NB Enschede, The Netherlands*

Complete contact information is available at:
https://pubs.acs.org/10.1021/acsnano.1c02495

Notes

The authors declare no competing financial interest.

ACKNOWLEDGMENTS

We appreciate the financial support of the Pioneers in Healthcare voucher (project Ischemia on chip) of the University of Twente, MST and ZGT in The Netherlands.

VOCABULARY

photonic crystal, a periodic optical nanostructure in which the index of refraction varies on the scale of the optical wavelength, affecting the flow of light; **photonic stop band**, a frequency range in which light cannot propagate in certain directions of the structure; **slow light**, the situation in which the group velocity of light is much reduced, something occurring at both the blue and red edges of a photonic stop band; **self-assembly**, one of the main "bottom-up" approaches, where building blocks such as molecules and colloids spontaneously organize into well-ordered structures by physical and/or chemical processes; **optical label-free sensor**, a sensor that can be used for quantification detection without the need for extra (*e.g.*, fluorescence) labels, for multiplexed sensing each sensor unit has its own encoded information that can be recognized by the specific optical spectrum; **sensitivity**, capability of the sensor to differentiate between two very close concentrations of analyte, concerning a change in sensor output per unit concentration/amount of analyte; **limit of detection**, the smallest concentration or amount of analyte that can be reliably detected and distinguished from the absence of that analyte by a specific measurement process

REFERENCES

(1) Ye, J.; Ouyang, S.; Chen, X.; Kako, T.; Zou, Z.; Li, Z. Enhanced Incident Photon-to-Electron Conversion Efficiency of Tungsten Trioxide Photoanodes Based on 3D-Photonic Crystal Design. *ACS Nano* **2011**, *5*, 4310−4318.

(2) Liu, J.; Zhao, H.; Wu, M.; Van der Schueren, B.; Li, Y.; Deparis, O.; Ye, J.; Ozin, G. A.; Hasan, T.; Su, B. L. Slow Photons for Photocatalysis and Photovoltaics. *Adv. Mater.* **2017**, *29*, 1605349.

(3) Burgess, I. B.; Mishchenko, L.; Hatton, B. D.; Kolle, M.; Loncar, M.; Aizenberg, J. Encoding Complex Wettability Patterns in Chemically Functionalized. *J. Am. Chem. Soc.* **2011**, *133*, 12430−12432.

(4) Wang, J.; Le-The, H.; Shui, L.; Bomer, J. G.; Jin, M.; Zhou, G.; Mulvaney, P.; Pinkse, P. W. H.; van den Berg, A.; Segerink, L. I.; Eijkel, J. C. T. Multilevel Spherical Photonic Crystals with Controllable Structures and Structure-Enhanced Functionalities. *Adv. Opt. Mater.* **2020**, *8*, 1902164.

(5) Hou, J.; Li, M.; Song, Y. Patterned Colloidal Photonic Crystals. *Angew. Chem., Int. Ed.* **2018**, *57*, 2544−2553.

(6) Zhao, Y.; Zhao, X.; Gu, Z. Photonic Crystals in Bioassays. *Adv. Funct. Mater.* **2010**, *20*, 2970−2988.

(7) Galisteo-Lopez, J. F.; Ibisate, M.; Sapienza, R.; Froufe-Perez, L. S.; Blanco, A.; Lopez, C. Self-Assembled Photonic Structures. *Adv. Mater.* **2011**, *23*, 30−69.

(8) Baba, T. Slow Light in Photonic Crystals. *Nat. Photonics* **2008**, *2*, 465−473.

(9) González-Urbina, L.; Baert, K.; Kolaric, B.; Pérez-Moreno, J.; Clays, K. Linear and Nonlinear Optical Properties of Colloidal Photonic Crystals. *Chem. Rev.* **2012**, *112*, 2268−2285.

(10) Fenzl, C.; Hirsch, T.; Wolfbeis, O. S. Photonic Crystals for Chemical Sensing and Biosensing. *Angew. Chem., Int. Ed.* **2014**, *53*, 3318−3335.

(11) Wongkaew, N.; Simsek, M.; Griesche, C.; Baeumner, A. J. Functional Nanomaterials and Nanostructures Enhancing Electrochemical Biosensors and Lab-on-a-Chip Performances: Recent Progress, Applications, and Future Perspective. *Chem. Rev.* **2019**, *119*, 120−194.

(12) Hildebrandt, N.; Spillmann, C. M.; Algar, W. R.; Pons, T.; Stewart, M. H.; Oh, E.; Susumu, K.; Diaz, S. A.; Delehanty, J. B.; Medintz, I. L. Energy Transfer with Semiconductor Quantum Dot Bioconjugates: A Versatile Platform for Biosensing, Energy Harvesting, and Other Developing Applications. *Chem. Rev.* **2017**, *117*, 536−711.

(13) Anker, J. N.; Hall, W. P.; Lyandres, O.; Shah, N. C.; Zhao, J.; Van Duyne, R. P. Biosensing with Plasmonic Nanosensors. *Nat. Mater.* **2008**, *7*, 442−453.

(14) Neubrech, F.; Huck, C.; Weber, K.; Pucci, A.; Giessen, H. Surface-Enhanced Infrared Spectroscopy Using Resonant Nanoantennas. *Chem. Rev.* **2017**, *117*, 5110−5145.

(15) Song, Y.; Bai, J.; Zhang, R.; He, H.; Li, C.; Wang, J.; Li, S.; Peng, Y.; Ning, B.; Wang, M.; Gao, Z. Michael-Addition-Mediated Photonic Crystals Allow Pretreatment- Free and Label-Free Sensoring of Ciprofloxacin in Fish Farming Water. *Anal. Chem.* **2018**, *90*, 1388−1394.

(16) Gargiulo, J.; Berte, R.; Li, Y.; Maier, S. A.; Cortes, E. From Optical to Chemical Hot Spots in Plasmonics. *Acc. Chem. Res.* **2019**, *52*, 2525−2535.

(17) Si, Y.; Sun, Z.; Zhang, N.; Qi, W.; Li, S.; Chen, L.; Wang, H. Ultrasensitive Electroanalysis of Low-Level Free MicroRNAs in Blood by Maximum Signal Amplification of Catalytic Silver Deposition Using Alkaline Phosphatase-Incorporated Gold Nanoclusters. *Anal. Chem.* **2014**, *86*, 10406−10414.

(18) Freeman, R.; Finder, T.; Bahshi, L.; Willner, I. β-Cyclodextrin-Modified CdSe/ZnS Quantum Dots for Sensing and Chiroselective Analysis. *Nano Lett.* **2009**, *9*, 2073−2076.

(19) Tokel, O.; Inci, F.; Demirci, U. Advances in Plasmonic Technologies for Point of Care Applications. *Chem. Rev.* **2014**, *114*, 5728−5752.

(20) Vogel, N.; Utech, S.; England, G. T.; Shirman, T.; Phillips, K. R.; Koay, N.; Burgess, I. B.; Kolle, M.; Weitz, D. A.; Aizenberg, J. Color from Hierarchy: Diverse Optical Properties of Micron-Sized Spherical Colloidal Assemblies. *Proc. Natl. Acad. Sci. U. S. A.* **2015**, *112*, 10845−10850.

(21) Pavarini, E.; Andreani, L.; Soci, C.; Galli, M.; Marabelli, F.; Comoretto, D. Band Structure and Optical Properties of Opal Photonic Crystals. *Phys. Rev. B: Condens. Matter Mater. Phys.* **2005**, *72*, 045102.

(22) Goerlitzer, E. S. A.; Klupp Taylor, R. N.; Vogel, N. Bioinspired Photonic Pigments from Colloidal Self-Assembly. *Adv. Mater.* **2018**, *30*, 1706654.

(23) Jones, A.; Dhanapala, L.; Kankanamage, R. N. T.; Kumar, C. V.; Rusling, J. F. Multiplexed Immunosensors and Immunoarrays. *Anal. Chem.* **2020**, *92*, 345−362.

(24) Deng, G.; Xu, K.; Sun, Y.; Chen, Y.; Zheng, T.; Li, J. High Sensitive Immunoassay for Multiplex Mycotoxin Detection with Photonic Crystal Microsphere Suspension Array. *Anal. Chem.* **2013**, *85*, 2833−2840.

(25) Míguez, H.; López, C.; Meseguer, F.; Blanco, A.; Vázquez, L.; Mayoral, R.; Ocaña, M.; Fornés, V.; Mifsud, A. Photonic Crystal Properties of Packed Submicrometric SiO_2 Spheres. *Appl. Phys. Lett.* **1997**, *71*, 1148−1150.

(26) Galisteo-López, J. F.; López, C. High-Energy Optical Response of Artificial Opals. *Phys. Rev. B: Condens. Matter Mater. Phys.* **2004**, *70*, 035108.

(27) Chen, J. I. L.; von Freymann, G.; Choi, S. Y.; Kitaev, V.; Ozin, G. A. Slow Photons in the Fast Lane in Chemistry. *J. Mater. Chem.* **2008**, *18*, 369−373.

(28) Li, M.; Lai, X.; Li, C.; Song, Y. Recent Advantages of Colloidal Photonic Crystals and Their Applications for Luminescence Enhancement. *Mater. Today Nano* **2019**, *6*, 100039.

(29) Nishimura, S.; Abrams, N.; Lewis, B. A.; Halaoui, L. I.; Mallouk, T. E.; Benkstein, K. D.; van de Lagemaat, J.; Frank, A. J. Standing Wave Enhancement of Red Absorbance and Photocurrent in Dye-Sensitized Titanium Dioxide Photoelectrodes Coupled to Photonic Crystals. *J. Am. Chem. Soc.* **2003**, *125*, 6306−6310.

(30) Sherry, L. J.; Jin, R.; Mirkin, C. A.; Schatz, G. C.; Van Duyne, R. P. Localized Surface Plasmon Resonance Spectroscopy of Single Silver Triangular Nanoprisms. *Nano Lett.* **2006**, *6*, 2060−2065.

(31) Tittl, A.; Leitis, A.; Liu, M.; Yesilkoy, F.; Choi, D. Y.; Neshev, D. N.; Kivshar, Y. S.; Altug, H. Imaging-Based Molecular Barcoding with Pixelated Dielectric Metasurfaces. *Science* **2018**, *360*, 1105−1109.

(32) Norris, D. J.; Arlinghaus, E. G.; Meng, L.; Heiny, R.; Scriven, L. E. Opaline Photonic Crystals: How Does Self-Assembly Work? *Adv. Mater.* **2004**, *16*, 1393−1399.

(33) Schaffner, M.; England, G.; Kolle, M.; Aizenberg, J.; Vogel, N. Combining Bottom-Up Self-Assembly with Top-Down Microfabrication to Create Hierarchical Inverse Opals with High Structural Order. *Small* **2015**, *11*, 4334−4340.

(34) Farka, Z.; Juřík, T.; Kovář, D.; Trnková, L.; Skládal, P. Nanoparticle-Based Immunochemical Biosensors and Assays: Recent Advances and Challenges. *Chem. Rev.* **2017**, *117*, 9973−10042.

(35) Lu, S.; Zhang, D. S.; Wei, D.; Lin, Y.; Zhang, S.; He, H.; Wei, X.; Gu, H.; Xu, H. Three-Dimensional Barcodes with Ultrahigh Encoding Capacities: A Flexible, Accurate, and Reproducible Encoding Strategy for Suspension Arrays. *Chem. Mater.* **2017**, *29*, 10398−10408.

(36) Rosman, C.; Prasad, J.; Neiser, A.; Henkel, A.; Edgar, J.; Sonnichsen, C. Multiplexed Plasmon Sensor for Rapid Label-Free Analyte Detection. *Nano Lett.* **2013**, *13*, 3243−3247.

(37) Zhao, Y.; Shang, L.; Cheng, Y.; Gu, Z. Spherical Colloidal Photonic Crystals. *Acc. Chem. Res.* **2014**, *47*, 3632−3642.

(38) Zhao, Y.; Zhao, X.; Tang, B.; Xu, W.; Li, J.; Hu, J.; Gu, Z. Quantum-Dot-Tagged Bioresponsive Hydrogel Suspension Array for Multiplex Label-Free DNA Detection. *Adv. Funct. Mater.* **2010**, *20*, 976−982.

(39) Hu, X.; Huang, J.; Zhang, W.; Li, M.; Tao, C.; Li, G. Photonic Ionic Liquids Polymer for Naked-Eye Anions. *Adv. Mater.* **2008**, *20*, 4074−4078.

(40) Wang, Y.; Li, W.; Li, M.; Zhao, S.; De Ferrari, F.; Liscidini, M.; Omenetto, F. G. Biomaterial-Based "Structured Opals" with Programmable Combination of Diffractive Optical Elements and Photonic Bandgap Effects. *Adv. Mater.* **2019**, *31*, 1805312.

(41) Chen, S.; Sun, H.; Huang, Z.; Jin, Z.; Fang, S.; He, J.; Liu, Y.; Zhang, Y.; Lai, J. The Visual Detection of Anesthetics in Fish Based on an Inverse Opal Photonic Crystal Sensor. *RSC Adv.* **2019**, *9*, 16831−16838.

(42) Zhao, Y.; Zhao, X.; Hu, J.; Xu, M.; Zhao, W.; Sun, L.; Zhu, C.; Xu, H.; Gu, Z. Encoded Porous Beads for Label-Free Multiplex Detection of Tumor Markers. *Adv. Mater.* **2009**, *21*, 569−572.

(43) Zhao, Y. J.; Zhao, X. W.; Hu, J.; Li, J.; Xu, W. Y.; Gu, Z. Z. Multiplex Label-Free Detection of Biomolecules with an Imprinted Suspension Array. *Angew. Chem., Int. Ed.* **2009**, *48*, 7350−7352.

(44) Xie, Z.; Cao, K.; Zhao, Y.; Bai, L.; Gu, H.; Xu, H.; Gu, Z. Z. An Optical Nose Chip Based on Mesoporous Colloidal Photonic Crystal Beads. *Adv. Mater.* **2014**, *26*, 2413−2418.

(45) Zhang, Y.; Sun, Y.; Liu, J.; Guo, P.; Cai, Z.; Wang, J. Polymer-Infiltrated SiO_2 Inverse Opal Photonic Crystals for Colorimetrically Selective Detection of Xylene Vapors. *Sens. Actuators, B* **2019**, *291*, 67−73.

(46) Li, L.; Jiao, X.; Chen, D.; Lotsch, B. V.; Li, C. Facile Fabrication of Ultrathin Metal-Organic Framework-Coated Monolayer Colloidal Crystals for Highly Efficient Vapor Sensing. *Chem. Mater.* **2015**, *27*, 7601−7609.

(47) Asher, S. A.; Sharma, A. C.; Goponenko, A. V.; Ward, M. M. Photonic Crystal Aqueous Metal Cation Sensing Materials. *Anal. Chem.* **2003**, *75*, 1676−1683.

(48) Moirangthem, M.; Arts, R.; Merkx, M.; Schenning, A. P. H. J. An Optical Sensor Based on a Photonic Polymer Film to Detect Calcium in Serum. *Adv. Funct. Mater.* **2016**, *26*, 1154−1160.

(49) Hong, W.; Hu, X.; Zhao, B.; Zhang, F.; Zhang, D. Tunable Photonic Polyelectrolyte Colorimetric Sensing for Anions, Cations and Zwitterions. *Adv. Mater.* **2010**, *22*, 5043−5047.

(50) Sharma, A. C.; Jana, T.; Kesavamoorthy, R.; Shi, L.; Virji, M. A.; Finegold, D. N.; Asher, S. A. A General Photonic Crystal Sensing Motif: Creatinine in Bodily Fluids. *J. Am. Chem. Soc.* **2004**, *126*, 2971−2977.

(51) Huang, C.; Cheng, Y.; Gao, Z.; Zhang, H.; Wei, J. Portable Label-Free Inverse Opal Photonic Hydrogel Particles Serve as Facile Pesticides Colorimetric Monitoring. *Sens. Actuators, B* **2018**, *273*, 1705−1712.

(52) Liu, C.; Zhang, W.; Zhao, Y.; Lin, C.; Zhou, K.; Li, Y.; Li, G. Urea-Functionalized Poly(ionic Liquid) Photonic Spheres for Visual Identification of Explosives with a Smartphone. *ACS Appl. Mater. Interfaces* **2019**, *11*, 21078−21085.

(53) Qin, J.; Li, X.; Cao, L.; Du, S.; Wang, W.; Yao, S. Q. Competition-Based Universal Photonic Crystal Biosensors by Using Antibody-Antigen Interaction. *J. Am. Chem. Soc.* **2020**, *142*, 417−423.

(54) Wang, Z.; Xue, M.; Zhang, H.; Meng, Z.; Shea, K. J.; Qiu, L.; Ji, T.; Xie, T. Self-Assembly of a Nano Hydrogel Colloidal Array for the Sensing of Humidity. *RSC Adv.* **2018**, *8*, 9963−9969.

(55) Choi, T. M.; Je, K.; Park, J. G.; Lee, G. H.; Kim, S. H. Photonic Capsule Sensors with Built-In Colloidal Crystallites. *Adv. Mater.* **2018**, *30*, 1803387.

(56) Chen, T.; Deng, Z.; Yin, S.; Chen, S.; Xu, C. The Fabrication of 2D and 3D Photonic Crystal Arrays towards High Performance Recognition of Metal Ions and Biomolecules. *J. Mater. Chem. C* **2016**, *4*, 1398−1404.

(57) Li, M.; He, F.; Liao, Q.; Liu, J.; Xu, L.; Jiang, L.; Song, Y.; Wang, S.; Zhu, D. Ultrasensitive DNA Detection Using Photonic Crystals. *Angew. Chem., Int. Ed.* **2008**, *47*, 7258−7262.

(58) Xu, Y.; Wang, H.; Luan, C.; Fu, F.; Chen, B.; Liu, H.; Zhao, Y. Porous Hydrogel Encapsulated Photonic Barcodes for Multiplex MicroRNA Quantification. *Adv. Funct. Mater.* **2018**, *28*, 1704458.

(59) Zhang, X.; Chen, G.; Bian, F.; Cai, L.; Zhao, Y. Encoded Microneedle Arrays for Detection of Skin Interstitial Fluid Biomarkers. *Adv. Mater.* **2019**, *31*, 1902825.

(60) Ji, J.; Lu, W.; Zhu, Y.; Jin, H.; Yao, Y.; Zhang, H.; Zhao, Y. Porous Hydrogel-Encapsulated Photonic Barcodes for Multiplex Detection of Cardiovascular Biomarkers. *ACS Sensors* **2019**, *4*, 1384−1390.

(61) Shao, C.; Chi, J.; Chen, Z.; Cai, L.; Zhao, Y. Superwettable Colloidal Crystal Micropatterns on Butterfly Wing Surface for Ultrasensitive Detection. *J. Colloid Interface Sci.* **2019**, *546*, 122−129.

(62) Zhao, Y.; Zhang, X.-J.; Ye, J.; Chen, L.-M.; Lau, S.-P.; Zhang, W.-J.; Lee, S.-T. Metallo-Dielectric Photonic Crystals for Surface-Enhanced Raman Scattering. *ACS Nano* **2011**, *5*, 3027−3033.

(63) Cai, Z.; Yan, Y.; Liu, L.; Lin, S.; Hu, X. Controllable Fabrication of Metallic Photonic Crystals for Ultra-Sensitive SERS and Photodetectors. *RSC Adv.* **2017**, *7*, 55851−55858.

(64) Qi, D.; Lu, L.; Wang, L.; Zhang, J. Improved SERS Sensitivity on Plasmon-Free TiO_2 Photonic Microarray by Enhancing Light-Matter Coupling. *J. Am. Chem. Soc.* **2014**, *136*, 9886−9889.

(65) Tan, Y.; Gu, J.; Xu, W.; Chen, Z.; Liu, D.; Liu, Q.; Zhang, D. Reduction of CuO Butterfly Wing Scales Generates Cu SERS Substrates for DNA Base Detection. *ACS Appl. Mater. Interfaces* **2013**, *5* (20), 9878−9882.

(66) Liu, B.; Zhao, X.; Jiang, W.; Fu, D.; Gu, Z. Multiplex Bioassays Encoded by Photonic Crystal Beads and SERS Nanotags. *Nanoscale* **2016**, *8*, 17465−17471.

(67) Liu, B.; Zhang, D.; Ni, H.; Wang, D.; Jiang, L.; Fu, D.; Han, X.; Zhang, C.; Chen, H.; Gu, Z.; Zhao, X. Multiplex Analysis on a Single Porous Hydrogel Bead with Encoded SERS Nanotags. *ACS Appl. Mater. Interfaces* **2018**, *10*, 21−26.

(68) Han, G. R.; Jang, C. H. Detection of Heavy-Metal Ions Using Liquid Crystal Droplet Patterns Modulated by Interaction between Negatively Charged Carboxylate and Heavy-Metal Cations. *Talanta* **2014**, *128*, 44−50.

(69) Kim, Y. J.; Park, S. Y. Optical Multisensor Array with Functionalized Photonic Droplets by an Interpenetrating Polymer Network for Human Blood Analysis. *ACS Appl. Mater. Interfaces* **2020**, *12*, 47342−47354.

(70) Lee, H.; Munir, S.; Park, S. Cholesteric Liquid Crystal Droplets for Biosensors. *ACS Appl. Mater. Interfaces* **2016**, *8*, 26407−26417.

(71) Verma, I.; Sidiq, S.; Pal, S. K. Poly(l -Lysine)-Coated Liquid Crystal Droplets for Sensitive Detection of DNA and Their Applications in Controlled Release of Drug Molecules. *ACS Omega* **2017**, *2*, 7936−7945.

(72) Bao, P.; Paterson, D. A.; Harrison, P. L.; Miller, K.; Peyman, S.; Jones, J. C.; Sandoe, J.; Evans, S. D.; Bushby, R. J.; Gleeson, H. F. Lipid Coated Liquid Crystal Droplets for the On-Chip Detection of Antimicrobial Peptides. *Lab Chip* **2019**, *19*, 1082−1089.

(73) Chang, C. K.; Kuo, H. L.; Tang, K. T.; Chiu, S. W. Optical Detection of Organic Vapors Using Cholesteric Liquid Crystals. *Appl. Phys. Lett.* **2011**, *99*, 073504.

(74) Hou, A.; Chen, H.; Zheng, C.; Xie, K.; Gao, A. Assembly of a Fluorescent Chiral Photonic Crystal Membrane and Its Sensitive Responses to Multiple Signals Induced by Small Molecules. *ACS Nano* **2020**, *14*, 7380−7388.

(75) Noh, K. G.; Park, S. Y. Smart Molecular-Spring Photonic Droplets. *Mater. Horiz.* **2017**, *4*, 633−640.

(76) Mayoral, R.; Requena, J.; Moya, J. S.; López, C.; Cintas, A.; Miguez, H.; Meseguer, F.; Vázquez, L.; Holgado, M.; Blanco, Á. 3D Long-Range Ordering in an SiO_2 Submicrometer-Sphere Sintered Superstructure. *Adv. Mater.* **1997**, *9*, 257−260.

(77) Aspnes, D. E. Optical Properties of Thin Films. *Thin Solid Films* **1982**, *89*, 249−262.

(78) Wu, P.; Wang, J.; Jiang, L. Bio-Inspired Photonic Crystal Patterns. *Mater. Horiz.* **2020**, *7*, 338−365.

(79) Li, H.; Chang, L.; Wang, J.; Yang, L.; Song, Y. A Colorful Oil-Sensitive Carbon Inverse Opal. *J. Mater. Chem.* **2008**, *18*, 5098−5103.

(80) Qian, W.; Gu, Z. Z.; Fujishima, A.; Sato, O. Three-Dimensionally Ordered Macroporous Polymer Materials: An Approach for Biosensor Applications. *Langmuir* **2002**, *18*, 4526−4529.

(81) Zhao, B. Y.; Zhao, X.; Hu, J.; Xu, M.; Zhao, W.; Sun, L.; Zhu, C.; Xu, H.; Gu, Z. Encoded Porous Beads for Label-Free Multiplex Detection of Tumor Markers. *Adv. Mater.* **2009**, *21*, 569−572.

(82) Xie, Z.; Cao, K.; Zhao, Y.; Bai, L.; Gu, H.; Xu, H.; Gu, Z. Z. An Optical Nose Chip Based on Mesoporous Colloidal Photonic Crystal Beads. *Adv. Mater.* **2014**, *26*, 2413−2418.

(83) Zhang, Y.; Qiu, J.; Hu, R.; Li, P.; Gao, L.; Heng, L.; Tang, B.; Jiang, L. A Visual and Organic Vapor Sensitive Photonic Crystal Sensor Consisting of Polymer-Infiltrated SiO_2 Inverse Opal. *Phys. Chem. Chem. Phys.* **2015**, *17*, 9651−9658.

(84) Burgess, I. B.; Mishchenko, L.; Hatton, B. D.; Kolle, M.; Lončar, M.; Aizenberg, J. Encoding Complex Wettability Patterns in Chemically Functionalized 3D Photonic Crystals. *J. Am. Chem. Soc.* **2011**, *133*, 12430−12432.

(85) Yu, Y.; Brandt, S.; Nicolas, N. J.; Aizenberg, J. Colorimetric Ethanol Indicator Based on Instantaneous, Localized Wetting of a Photonic Crystal. *ACS Appl. Mater. Interfaces* **2020**, *12*, 1924−1929.

(86) Heshmat, M.; Li, P. C. H. Construction of an Array of Photonic Crystal Films for Visual Differentiation of Water/Ethanol Mixtures. *ACS Omega* **2019**, *4*, 19991−19999.

(87) Christodoulides, N.; Mohanty, S.; Miller, C. S.; Langub, M. C.; Floriano, P. N.; Dharshan, P.; Ali, M. F.; Bernard, B.; Romanovicz, D.; Anslyn, E.; Fox, P.; McDevitt, J. Application of Microchip Assay System for the Measurement of C-Reactive Protein in Human Saliva. *Lab Chip* **2005**, *5*, 261−269.

(88) Zhang, Y.; Fu, Q.; Ge, J. Photonic Sensing of Organic Solvents through Geometric Study of Dynamic Reflection Spectrum Geometric Study of Dynamic Reflection Spectrum. *Nat. Commun.* **2015**, *6*, 7510.

(89) Xiao, F.; Sun, Y.; Du, W.; Shi, W.; Wu, Y.; Liao, S.; Wu, Z.; Yu, R. Smart Photonic Crystal Hydrogel Material for Uranyl Ion Monitoring and Removal in Water. *Adv. Funct. Mater.* **2017**, *27*, 1702147.

(90) Zhu, Y.; Wang, J.; Zhu, X.; Wang, J.; Zhou, L.; Li, J.; Mei, T.; Qian, J.; Wei, L.; Wang, X. Carbon Dot-Based Inverse Opal Hydrogels with Photoluminescence: Dual-Mode Sensing of Solvents and Metal Ions. *Analyst* **2019**, *144*, 5802−5809.

(91) Macconaghy, K. I.; Geary, C. I.; Kaar, J. L.; Stoykovich, M. P. Photonic Crystal Kinase Biosensor. *J. Am. Chem. Soc.* **2014**, *136*, 6896−6899.

(92) Goponenko, A. V.; Asher, S. A. Modeling of Stimulated Hydrogel Volume Changes in Photonic Crystal Pb^{2+} Sensing Materials. *J. Am. Chem. Soc.* **2005**, *127*, 10753−10759.

(93) Lee, K.; Asher, S. A. Photonic Crystal Chemical Sensors: PH and Ionic Strength. *J. Am. Chem. Soc.* **2000**, *122*, 9534−9537.

(94) Qin, J.; Dong, B.; Li, X.; Han, J.; Gao, R.; Su, G.; Cao, L.; Wang, W. Fabrication of Intelligent Photonic Crystal Hydrogel Sensors for Selective Detection of Trace Mercury Ions in Seawater. *J. Mater. Chem. C* **2017**, *5*, 8482−8488.

(95) Arunbabu, D.; Sannigrahi, A.; Jana, T. Photonic Crystal Hydrogel Material for the Sensing of Toxic Mercury Ions (Hg^{2+}) in Water. *Soft Matter* **2011**, *7*, 2592−2599.

(96) Ye, B.; Ding, H.; Cheng, Y.; Gu, H.; Zhao, Y.; Xie, Z.; Gu, Z. Photonic Crystal Microcapsules for Label-Free Multiplex Detection. *Adv. Mater.* **2014**, *26*, 3270−3274.

(97) Qin, J.; Dong, B.; Cao, L.; Wang, W. Photonic Hydrogels for the Ultratrace Sensing of Divalent Beryllium in Seawater. *J. Mater. Chem. C* **2018**, *6*, 4234−4242.

(98) Leo, S.; Zhang, W.; Zhang, Y.; Ni, Y.; Jiang, H.; Jones, C.; Jiang, P.; Basile, V.; Taylor, C. Chromogenic Photonic Crystal Sensors Enabled by Multistimuli-Responsive Shape Memory Polymers. *Small* **2018**, *14*, 1703515.

(99) Zhang, Y.; Ge, J. Liquid Photonic Crystal Detection Reagent for Reliable Sensing of Cu^{2+} in Water. *RSC Adv.* **2020**, *10*, 10972−10979.

(100) Chang, P.; Niu, W.; Qu, L.; Zhang, S. Two-Way Rewritable and Stable Photonic Patterns Enabled by Near-Infrared Laser-Responsive Shape Memory Photonic Crystals. *J. Mater. Chem. C* **2019**, *7*, 1896−1903.

(101) Fang, Y.; Leo, S. Y.; Ni, Y.; Wang, J.; Wang, B.; Yu, L.; Dong, Z.; Dai, Y.; Basile, V.; Taylor, C.; Jiang, P. Reconfigurable Photonic Crystals Enabled by Multistimuli-Responsive Shape Memory Polymers Possessing Room Temperature Shape Processability. *ACS Appl. Mater. Interfaces* **2017**, *9*, 5457−5467.

(102) Fang, Y.; Ni, Y.; Leo, S. Y.; Taylor, C.; Basile, V.; Jiang, P. Reconfigurable Photonic Crystals Enabled by Pressure-Responsive Shape-Memory Polymers. *Nat. Commun.* **2015**, *6*, 7416.

(103) Inan, H.; Poyraz, M.; Inci, F.; Lifson, M. A.; Baday, M.; Cunningham, B. T.; Demirci, U. Photonic Crystals: Emerging Biosensors and Their Promise for Point-of-Care Applications. *Chem. Soc. Rev.* **2017**, *46*, 366−388.

(104) Sun, J.; Xianyu, Y.; Jiang, X. Point-of-Care Biochemical Assays Using Gold Nanoparticle-Implemented Microfluidics. *Chem. Soc. Rev.* **2014**, *43*, 6239−6253.

(105) Kim, H. N.; Ren, W. X.; Kim, J. S.; Yoon, J. Fluorescent and Colorimetric Sensors for Detection of Lead, Cadmium, and Mercury Ions. *Chem. Soc. Rev.* **2012**, *41*, 3210−3244.

(106) Medintz, I. L.; Clapp, A. R.; Mattoussi, H.; Goldman, E. R.; Fisher, B.; Mauro, J. M. Self-Assembled Nanoscale Biosensors Based on Quantum Dot FRET Donors. *Nat. Mater.* **2003**, *2*, 630−638.

(107) Medintz, I. L.; Clapp, A. R.; Brunel, F. M.; Tiefenbrunn, T.; Tetsuo Uyeda, H.; Chang, E. L.; Deschamps, J. R.; Dawson, P. E.; Mattoussi, H. Proteolytic Activity Monitored by through Quantum-Dot-Peptide Conjugates. *Nat. Mater.* **2006**, *5*, 581−589.

(108) Ganesh, N.; Zhang, W.; Mathias, P. C.; Chow, E.; Soares, J. A. N. T.; Malyarchuk, V.; Smith, A. D.; Cunningham, B. T. Enhanced Fluorescence Emission from Quantum Dots on a Photonic Crystal Surface. *Nat. Nanotechnol.* **2007**, *2*, 515−520.

(109) Wei, X.; Bian, F.; Cai, X.; Wang, Y.; Cai, L.; Yang, J.; Zhu, Y.; Zhao, Y. Multiplexed Detection Strategy for Bladder Cancer MicroRNAs Based on Photonic Crystal Barcodes. *Anal. Chem.* **2020**, *92*, 6121−6127.

(110) Eftekhari, E.; Wang, W.; Li, X.; A, N.; Wu, Z.; Klein, R.; Cole, I. S.; Li, Q. Picomolar Reversible Hg (II) Solid-State Sensor Based on Carbon Dots in Double Heterostructure Colloidal Photonic Crystals. *Sens. Actuators, B* **2017**, *240*, 204−211.

(111) Qin, M.; Huang, Y.; Li, Y.; Su, M.; Chen, B.; Sun, H.; Yong, P.; Ye, C.; Li, F.; Song, Y. Rainbow Structural-Color Chip for Multisaccharide Recognition. *Angew. Chem., Int. Ed.* **2016**, *55*, 6911−6914.

(112) Li, J.; Yang, P.; Huang, R.; Huo, D.; Hou, C. A Microarray Chip Based on Photonic Crystals and Fluorescence Ampli Fi Cation for Discrimination of Baijiu. *Anal. Methods* **2019**, *11*, 5413−5420.

(113) Zhao, Y.; Zhao, X.; Sun, C.; Li, J.; Zhu, R.; Gu, Z. Encoded Silica Colloidal Crystal Beads as Supports for Potential Multiplex Immunoassay. *Anal. Chem.* **2008**, *80*, 1598−1605.

(114) Aravindakshan, N.; Eftekhari, E.; Tan, S. H.; Li, X.; St John, J.; Nguyen, N. T.; Zhao, H.; Zhao, D.; Li, Q. Ensembles of Photonic Beads: Optical Properties and Enhanced Light-Matter Interactions. *Adv. Opt. Mater.* **2020**, *8*, 1901537.

(115) Zhang, L.; Wang, J.; Tao, S.; Geng, C.; Yan, Q. Universal Fluorescence Enhancement Substrate Based on Multiple Heterostructure Photonic Crystal with Super-Wide Stopband and Highly Sensitive Cr(VI) Detecting Performance. *Adv. Opt. Mater.* **2018**, *6*, 1701344.

(116) Zheng, F.; Cheng, Y.; Wang, J.; Lu, J.; Zhang, B.; Zhao, Y.; Gu, Z. Aptamer-Functionalized Barcode Particles for the Capture and Detection of Multiple Types of Circulating Tumor Cells. *Adv. Mater.* **2014**, *26*, 7333−7338.

(117) Liu, S.; Zhang, X.; Luo, W.; Wang, Z.; Guo, X.; Steigerwald, M. L.; Fang, X. Single-Molecule Detection of Proteins Using Aptamer-Functionalized Molecular Electronic Devices. *Angew. Chem., Int. Ed.* **2011**, *50*, 2496−2502.

(118) Ma, X.; Zhao, Z.; Wang, H.; Liu, Y.; Xu, Y.; Zhang, J.; Chen, B.; Li, L.; Zhao, Y. P-Glycoprotein Antibody Decorated Porous Hydrogel Particles for Capture and Release of Drug-Resistant Tumor Cells. *Adv. Healthcare Mater.* **2019**, *8*, 1900136.

(119) Tang, B.; Zhao, X.; Zhao, Y.; Zhang, W.; Wang, Q.; Kong, L.; Gu, Z. Binary Optical Encoding Strategy for Multiplex Assay. *Langmuir* **2011**, *27*, 11722−11728.

(120) Leng, Y.; Sun, K.; Chen, X.; Li, W. Suspension Arrays Based on Nanoparticle-Encoded Microspheres for High-Throughput Multiplexed Detection. *Chem. Soc. Rev.* **2015**, *44*, 5552−5595.

(121) Zhong, K.; Song, K.; Clays, K. Hollow Spheres: Crucial Building Blocks for Novel Nanostructures and Nanophotonics. *Nanophotonics* **2018**, *7*, 693−713.

(122) Wang, Y.; Shang, L.; Bian, F.; Zhang, X.; Wang, S.; Zhou, M.; Zhao, Y. Hollow Colloid Assembled Photonic Crystal Clusters as Suspension Barcodes for Multiplex Bioassays. *Small* **2019**, *15*, 1900056.

(123) Zhong, K.; Khorshid, M.; Li, J.; Markey, K.; Wagner, P. H.; Song, K.; Van Cleuvenbergen, S.; Clays, K. Fabrication of Optomicrofluidics for Real-Time Bioassays Based on Hollow Sphere Colloidal Photonic Crystals with Wettability Patterns. *J. Mater. Chem. C* **2016**, *4*, 7853−7858.

(124) Ali, M. M.; Li, F.; Zhang, Z.; Zhang, K.; Kang, D. K.; Ankrum, J. A.; Le, X. C.; Zhao, W. Rolling Circle Amplification: A Versatile Tool for Chemical Biology, Materials Science and Medicine. *Chem. Soc. Rev.* **2014**, *43*, 3324−3341.

(125) Zhang, D.; Bian, F.; Cai, L.; Wang, T.; Kong, T.; Zhao, Y. Bioinspired Photonic Barcodes for Multiplexed Target Cycling and Hybridization Chain Reaction. *Biosens. Bioelectron.* **2019**, *143*, 111629.

(126) Bian, F.; Wu, J.; Wang, H.; Sun, L.; Shao, C.; Wang, Y.; Li, Z.; Wang, X.; Zhao, Y. Bioinspired Photonic Barcodes with Graphene Oxide Encapsulation for Multiplexed MicroRNA Quantification. *Small* **2018**, *14*, 1803551.

(127) Cai, L.; Bian, F.; Sun, L.; Wang, H.; Zhao, Y. Condensing-Enriched Magnetic Photonic Barcodes on Superhydrophobic Surface for Ultrasensitive Multiple Detection. *Lab Chip* **2019**, *19*, 1783−1789.

(128) Hou, J.; Zhang, H.; Yang, Q.; Li, M.; Song, Y.; Jiang, L. Bio-Inspired Photonic-Crystal Microchip for Fluorescent Ultratrace Detection. *Angew. Chem., Int. Ed.* **2014**, *53*, 5791−5795.

(129) Zhang, D.; Cai, L.; Bian, F.; Kong, T.; Zhao, Y. Label-Free Quantifications of Multiplexed Mycotoxins by G-Quadruplex Based on Photonic Barcodes. *Anal. Chem.* **2020**, *92*, 2891−2895.

(130) Huang, Y.; Li, F.; Qin, M.; Jiang, L.; Song, Y. A Multi-Stopband Photonic-Crystal Microchip for High-Performance Metal-Ion Recognition Based on Fluorescent Detection. *Angew. Chem., Int. Ed.* **2013**, *52*, 7296−7299.

(131) Palacios, M. A.; Wang, Z.; Montes, V. A.; Zyryanov, G. V.; Anzenbacher, P. Rational Design of a Minimal Size Sensor Array for Metal Ion Detection. *J. Am. Chem. Soc.* **2008**, *130*, 10307−10314.

(132) Yu, J.; Zhang, Y.; Ye, Y.; DiSanto, R.; Sun, W.; Ranson, D.; Ligler, F. S.; Buse, J. B.; Gu, Z. Microneedle-Array Patches Loaded with Hypoxia-Sensitive Vesicles Provide Fast Glucose-Responsive Insulin Delivery. *Proc. Natl. Acad. Sci. U. S. A.* **2015**, *112*, 8260−8265.

(133) Tang, J.; Wang, J.; Huang, K.; Ye, Y.; Su, T.; Qiao, L.; Hensley, M. T.; Caranasos, T. G.; Zhang, J.; Gu, Z.; Cheng, K. Cardiac Cell-Integrated Microneedle Patch for Treating Myocardial Infarction. *Sci. Adv.* **2018**, *4*, No. eaat9365.

(134) Bian, F.; Sun, L.; Cai, L.; Wang, Y.; Zhao, Y.; Wang, S.; Zhou, M. Molybdenum Disul Fi De-Integrated Photonic Barcodes for Tumor Markers Screening. *Biosens. Bioelectron.* **2019**, *133*, 199−204.

(135) Bell, S. E. J.; Charron, G.; Cortes, E.; Kneipp, J.; Chapelle, M. L.; Langer, J.; Prochazka, M.; Tran, V.; Schlucker, S. Towards Reliable and Quantitative Surface-Enhanced Raman Scattering (SERS): From Key Parameters to Good Analytical Practice Angewandte. *Angew. Chem., Int. Ed.* **2020**, *59*, 5454−5462.

(136) Dugandžić, V.; Kupfer, S.; Jahn, M.; Henkel, T.; Weber, K.; Cialla-May, D.; Popp, J. A SERS-Based Molecular Sensor for Selective Detection and Quantification of Copper (II) Ions. *Sens. Actuators, B* **2019**, *279*, 230−237.

(137) Chung, E.; Gao, R.; Ko, J.; Choi, N.; Lim, D. W.; Lee, E. K.; Chang, S.-I.; Choo, J. Lab on a Chip Trace Analysis of Mercury (II) Ions Using Aptamer-Modified Au/Ag Core-Shell Nanoparticles and SERS Spectroscopy in a Microdroplet Channel. *Lab Chip* **2013**, *13*, 260−266.

(138) Le Thi Ngoc, L.; Jin, M.; Wiedemair, J.; van den Berg, A.; Carlen, E. T. Large Area Metal Nanowire Arrays with Tunable Sub-20 nm Nanogaps. *ACS Nano* **2013**, *7*, 5223−5234.

(139) Cao, Y. C.; Jin, R.; Mirkin, C. A. Nanoparticles with Raman Spectroscopic Fingerprints for DNA and RNA Detection. *Science* **2002**, *297*, 1536−1541.

(140) Kim, W. H.; Lee, J. U.; Song, S.; Kim, S.; Choi, Y. J.; Sim, S. J. A Label-Free, Ultra-Highly Sensitive and Multiplexed SERS Nanoplasmonic Biosensor for MiRNA Detection Using a Head-Flocked Gold Nanopillar. *Analyst* **2019**, *144*, 1768−1776.

(141) Vo-Dinh, T.; Allain, L. R.; Stokes, D. L. Cancer Gene Detection Using Surface-Enhanced Raman Scattering (SERS). *J. Raman Spectrosc.* **2002**, *33*, 511−516.

(142) Zhang, Y.; Yang, P.; Habeeb Muhammed, M. A.; Alsaiari, S. K.; Moosa, B.; Almalik, A.; Kumar, A.; Ringe, E.; Khashab, N. M. Tunable and Linker Free Nanogaps in Core-Shell Plasmonic Nanorods for Selective and Quantitative Detection of Circulating Tumor Cells by SERS. *ACS Appl. Mater. Interfaces* **2017**, *9*, 37597−37605.

(143) Cialla-May, D.; Zheng, X.-S.; Weber, K.; Popp, J. Recent Progress in Surface-Enhanced Raman Spectroscopy for Biological and Biomedical Applications: From Cells to Clinics. *Chem. Soc. Rev.* **2017**, *46*, 3945−3961.

(144) Lee, Y. H.; Shi, W.; Lee, H. K.; Jiang, R.; Phang, I. Y.; Cui, Y.; Isa, L.; Yang, Y.; Wang, J.; Li, S.; Ling, X. Nanoscale Surface Chemistry Directs the Tunable Assembly of Silver Octahedra into Three Two-Dimensional Plasmonic Superlattices. *Nat. Commun.* **2015**, *6*, 6990.

(145) Langer, J.; Jimenez De Aberasturi, D.; Aizpurua, J.; Alvarez-Puebla, R. A.; Auguié, B.; Baumberg, J. J.; Bazan, G. C.; Bell, S. E. J.; Boisen, A.; Brolo, A. G.; Choo, J.; Cialla-May, D.; Deckert, V.; Fabris, L.; Faulds, K.; García de Abajo, F. J.; Goodacre, R.; Graham, D.; Haes, A.; Haynes, C.; et al. Present and Future of Surface-Enhanced Raman Scattering. *ACS Nano* **2020**, *14*, 28−117.

(146) Lee, H. K.; Lee, Y. H.; Koh, C. S. L.; Phan-Quang, G. C.; Han, X.; Lay, C. L.; Sim, H. Y. F.; Kao, Y.-C.; An, Q.; Ling, X. Y. Designing Surface-Enhanced Raman Scattering (SERS) Platforms beyond

Hotspot Engineering: Emerging Opportunities in Analyte Manipulations and Hybrid Materials. *Chem. Soc. Rev.* **2019**, *48*, 731−756.

(147) Tian, S.; Neumann, O.; Mcclain, M. J.; Yang, X.; Zhou, L.; Zhang, C.; Nordlander, P.; Halas, N. J. Aluminum Nanocrystals: A Sustainable Substrate for Quantitative SERS-Based DNA Detection. *Nano Lett.* **2017**, *17*, 5071−5077.

(148) Lee, Y. H.; Lay, C. L.; Shi, W.; Lee, H. K.; Yang, Y.; Li, S.; Ling, X. Y. Creating Two Self-Assembly Micro-Environments to Achieve Supercrystals with Dual Structures Using Polyhedral Nanoparticles. *Nat. Commun.* **2018**, *9*, 2769.

(149) Hong, Y.; Qiu, Y.; Chen, T.; Reinhard, B. M. Rational Assembly of Optoplasmonic Hetero-Nanoparticle Arrays with Tunable Photonic-Plasmonic Resonances. *Adv. Funct. Mater.* **2014**, *24*, 739−746.

(150) Wang, J.; Jin, M.; Gong, Y.; Li, H.; Wu, S.; Zhang, Z.; Zhou, G.; Shui, L.; Eijkel, J. C. T.; van den Berg, A. Continuous Fabrication of Microcapsules with Controllable Metal Covered Nanoparticle Arrays Using Droplet Microfluidics for Localized Surface Plasmon Resonance. *Lab Chip* **2017**, *17*, 1970−1979.

(151) Wang, J.; Le-The, H.; Karamanos, T.; Suryadharma, R. N. S.; Van Den Berg, A.; Pinkse, P. W. H.; Rockstuhl, C.; Shui, L.; Eijkel, J. C. T.; Segerink, L. I. Plasmonic Nanocrystal Arrays on Photonic Crystals with Tailored Optical Resonances. *ACS Appl. Mater. Interfaces* **2020**, *12*, 37657−37669.

(152) Kuang, M.; Wang, J.; Jiang, L. Bio-Inspired Photonic Crystals with Superwettability. *Chem. Soc. Rev.* **2016**, *45*, 6833−6854.

(153) De Angelis, F.; Gentile, F.; Mecarini, F.; Das, G.; Moretti, M.; Candeloro, P.; Coluccio, M. L.; Cojoc, G.; Accardo, A.; Liberale, C.; Zaccaria, R. P.; Perozziello, G.; Tirinato, L.; Toma, A.; Cuda, G.; Cingolani, R.; Di Fabrizio, E. Breaking the Diffusion Limit with Super-Hydrophobic Delivery of Molecules to Plasmonic Nanofocusing SERS Structures. *Nat. Photonics* **2011**, *5*, 682−687.

(154) Hwang, H.; Kim, S. H.; Yang, S. M. Microfluidic Fabrication of SERS-Active Microspheres for Molecular Detection. *Lab Chip* **2011**, *11*, 87−92.

(155) Guddala, S.; Kamanoor, S. A.; Chiappini, A.; Ferrari, M.; Desai, N. R. Experimental Investigation of Photonic Band Gap Influence on Enhancement of Raman-Scattering in Metal-Dielectric Colloidal Crystals. *J. Appl. Phys.* **2012**, *112*, 084303.

(156) Sivashanmugan, K.; Squire, K.; Kraai, J. A.; Tan, A.; Zhao, Y.; Rorrer, G. L.; Wang, A. X. Biological Photonic Crystal-Enhanced Plasmonic Mesocapsules: Approaching Single-Molecule Optofluidic-SERS Sensing. *Adv. Opt. Mater.* **2019**, *7*, 1900415.

(157) Mu, Z.; Zhao, X.; Huang, Y.; Lu, M.; Gu, Z. Photonic Crystal Hydrogel Enhanced Plasmonic Staining for Multiplexed Protein Analysis. *Small* **2015**, *11*, 6036−6043.

(158) Chen, G.; Zhang, K.; Luo, B.; Hong, W.; Chen, J.; Chen, X. Plasmonic-3D Photonic Crystals Microchip for Surface Enhanced Raman Spectroscopy. *Biosens. Bioelectron.* **2019**, *143*, 111596.

(159) Phillips, K. R.; Shirman, T.; Shirman, E.; Shneidman, A. V.; Kay, T. M.; Aizenberg, J. Nanocrystalline Precursors for the Co-Assembly of Crack-Free Metal Oxide Inverse Opals. *Adv. Mater.* **2018**, *30*, 1706329.

(160) Tadepalli, S.; Slocik, J. M.; Gupta, M. K.; Naik, R. R.; Singamaneni, S. Bio-Optics and Bio-Inspired Optical Materials. *Chem. Rev.* **2017**, *117*, 12705−12763.

(161) Tan, Y.; Gu, J.; Xu, L.; Zang, X.; Liu, D.; Zhang, W.; Liu, Q.; Zhu, S.; Su, H.; Feng, C.; Fan, G.; Zhang, D. High-Density Hotspots Engineered by Naturally Piled-Up Subwavelength Structures in Three-Dimensional Copper Butterfly Wing Scales for Surface-Enhanced Raman Scattering Detection. *Adv. Funct. Mater.* **2012**, *22*, 1578−1585.

(162) Palmer, L. D.; Brooks, J. L.; Frontiera, R. R. Probing the Coupling of Butterfly Wing Photonic Crystals to Plasmon Resonances with Surface-Enhanced Raman Spectroscopy. *J. Mater. Chem. C* **2019**, *7*, 13887−13895.

(163) Ren, F.; Campbell, J.; Wang, X.; Rorrer, G. L.; Wang, A. X. Enhancing Surface Plasmon Resonances of Metallic Nanoparticles by Diatom Biosilica. *Opt. Express* **2013**, *21*, 15308−15313.

(164) Lin, S.; Zhu, W.; Jin, Y.; Crozier, K. B. Surface-Enhanced Raman Scattering with Ag Nanoparticles Optically Trapped by a Photonic Crystal Cavity. *Nano Lett.* **2013**, *13*, 559−563.

(165) Zhang, C.; Wang, H.; Guan, S.; Guo, Z.; Zheng, X.; Fan, Y.; Wang, Y.; Qu, T.; Zhao, Y.; Chen, A.; Zhu, G.; Wang, Z. Self-Powered Optical Switch Based on Triboelectrification-Triggered Liquid Crystal Alignment for Wireless Sensing. *Adv. Funct. Mater.* **2019**, *29*, 1808633.

(166) Noh, K.-G.; Park, S.-Y. Biosensor Array of Interpenetrating Polymer Network with Photonic Film Templated from Reactive Cholesteric Liquid Crystal and Enzyme-Immobilized Hydrogel Polymer. *Adv. Funct. Mater.* **2018**, *28*, 1707562.

(167) Yang, S.; Wu, C.; Tan, H.; Wu, Y.; Liao, S.; Wu, Z.; Shen, G.; Yu, R. Label-Free Liquid Crystal Biosensor Based on Specific Oligonucleotide Probes for Heavy Metal Ions. *Anal. Chem.* **2013**, *85*, 14−18.

(168) Brake, J. M.; Mezera, A. D.; Abbott, N. L. Effect of Surfactant Structure on the Orientation of Liquid Crystals at Aqueous-Liquid Crystal Interfaces. *Langmuir* **2003**, *19*, 6436−6442.

(169) Munir, S.; Park, S. Y. Liquid Crystal-Based DNA Biosensor for Myricetin Detection. *Sens. Actuators, B* **2016**, *233*, 559−565.

(170) Zhou, L.; Hu, Q.; Kang, Q.; Fang, M.; Yu, L. Construction of a Liquid Crystal-Based Sensing Platform for Sensitive and Selective Detection of l-Phenylalanine Based on Alkaline Phosphatase. *Langmuir* **2019**, *35*, 461−467.

(171) Meli, M. V.; Lin, I. H.; Abbott, N. L. Preparation of Microscopic and Planar Oil-Water Interfaces That Are Decorated with Prescribed Densities of Insoluble Amphiphiles. *J. Am. Chem. Soc.* **2008**, *130*, 4326−4333.

(172) Sivakumar, S.; Wark, K. L.; Gupta, J. K.; Abbott, N. L.; Caruso, F. Liquid Crystal Emulsions as the Basis of Biological Sensors for the Optical Detection of Bacteria and Viruses. *Adv. Funct. Mater.* **2009**, *19*, 2260−2265.

(173) Manna, U.; Zayas-Gonzalez, Y. M.; Carlton, R. J.; Caruso, F.; Abbott, N. L.; Lynn, D. M. Liquid Crystal Chemical Sensors That Cells Can Wear. *Angew. Chem., Int. Ed.* **2013**, *52*, 14011−14015.

(174) Bedolla Pantoja, M. A.; Abbott, N. L. Surface-Controlled Orientational Transitions in Elastically Strained Films of Liquid Crystal That Are Triggered by Vapors of Toluene. *ACS Appl. Mater. Interfaces* **2016**, *8*, 13114−13122.

(175) Bisoyi, H. K.; Li, Q. Light-Directing Chiral Liquid Crystal Nanostructures: From 1D to 3D. *Acc. Chem. Res.* **2014**, *47*, 3184−3195.

(176) Tjipto, E.; Cadwell, K. D.; Quinn, J. F.; Johnston, A. P. R.; Abbott, N. L.; Caruso, F. Tailoring the Interfaces between Nematic Liquid Crystal Emulsions and Aqueous Phases *via* Layer-by-Layer Assembly. *Nano Lett.* **2006**, *6*, 2243−2248.

(177) Shibaev, P. V.; Roslyak, O.; Gullatt, E.; Plumitallo, J.; Aparajita, U. Liquid Crystal Nose Based on Chiral Photonic Band Gap Materials: Principles of Selective Response. *Appl. Phys. A: Mater. Sci. Process.* **2020**, *126*, 920.

(178) Chen, H.; Hou, A.; Zheng, C.; Tang, J.; Xie, K.; Gao, A. Light- and Humidity-Responsive Chiral Nematic Photonic Crystal Films Based on Cellulose Nanocrystals. *ACS Appl. Mater. Interfaces* **2020**, *12*, 24505−24511.

(179) Zheng, Z. G.; Li, Y.; Bisoyi, H. K.; Wang, L.; Bunning, T. J.; Li, Q. Three-Dimensional Control of the Helical Axis of a Chiral Nematic Liquid Crystal by Light. *Nature* **2016**, *531*, 352−356.

(180) Broer, D. J.; Bastiaansen, C. M. W.; Debije, M. G.; Schenning, A. P. H. J. Functional Organic Materials Based on Polymerized Liquid-Crystal Monomers: Supramolecular Hydrogen-Bonded Systems. *Angew. Chem., Int. Ed.* **2012**, *51*, 7102−7109.

(181) Martinez, A. M.; McBride, M. K.; White, T. J.; Bowman, C. N. Reconfigurable and Spatially Programmable Chameleon Skin-Like Material Utilizing Light Responsive Covalent Adaptable Cholesteric Liquid Crystal Elastomers. *Adv. Funct. Mater.* **2020**, *30*, 2003150.

(182) Kim, J.; Khan, M.; Park, S. Glucose Sensor Using Liquid-Crystal Droplets Made by Micro Fluidics. *ACS Appl. Mater. Interfaces* **2013**, *5*, 13135−13139.

(183) Lee, H. G.; Munir, S.; Park, S. Y. Cholesteric Liquid Crystal Droplets for Biosensors. *ACS Appl. Mater. Interfaces* **2016**, *8*, 26407−26417.

(184) Sidiq, S.; Prasad, G. V. R. K.; Mukhopadhaya, A.; Pal, S. K. Poly(L-lysine)-Coated LC Droplets Cell-Based Sensing. *J. Phys. Chem. B* **2017**, *121*, 4247−4256.

(185) Guo, X.; Manna, U.; Abbott, N. L.; Lynn, D. M. Covalent Immobilization of Caged Liquid Crystal Microdroplets on Surfaces. *ACS Appl. Mater. Interfaces* **2015**, *7*, 26892−26903.

(186) Tang, S. K. Y.; Li, Z.; Abate, A. R.; Agresti, J. J.; Weitz, D. A.; Psaltis, D.; Whitesides, G. M. A Multi-Color Fast-Switching Microfluidic Droplet Dye Laser. *Lab Chip* **2009**, *9*, 2767−2771.

(187) Zhao, L.; Wang, Y.; Yuan, Y.; Liu, Y.; Liu, S.; Sun, W.; Yang, J.; Li, H. Whispering Gallery Mode Laser Based on Cholesteric Liquid Crystal Microdroplets as Temperature Sensor. *Opt. Commun.* **2017**, *402*, 181−185.

(188) Kim, J.; Park, S. Photonic Spring-Like Shell Templated from Cholesteric Liquid Crystal Prepared by Microfluidics. *Adv. Opt. Mater.* **2017**, *5*, 1700243.

(189) Lim, J. S.; Kim, Y. J.; Park, S. Y. Functional Solid-State Photonic Droplets with Interpenetrating Polymer Network and Their Applications to Biosensors. *Sens. Actuators, B* **2021**, *329*, 129165.

(190) Stumpel, J. E.; Broer, D. J.; Schenning, A. P. H. J. Water-Responsive Dual-Coloured Photonic Polymer Coatings Based on Cholesteric Liquid Crystals. *RSC Adv.* **2015**, *5*, 94650−94653.

(191) Revol, J. F.; Bradford, H.; Giasson, J.; Marchessault, R. H.; Gray, D. G. Helicoidal Self-Ordering of Cellulose Microfibrils in Aqueous Suspension. *Int. J. Biol. Macromol.* **1992**, *14* (3), 170−172.

(192) Shopsowitz, K. E.; Qi, H.; Hamad, W. Y.; MacLachlan, M. J. Free-Standing Mesoporous Silica Films with Tunable Chiral Nematic Structures. *Nature* **2010**, *468*, 422−426.

(193) Guidetti, G.; Atifi, S.; Vignolini, S.; Hamad, W. Y. Flexible Photonic Cellulose Nanocrystal Films. *Adv. Mater.* **2016**, *28*, 10042−10047.

(194) Bai, L.; Wang, Z. L.; He, Y. D.; Song, F.; Wang, X. L.; Wang, Y. Z. Flexible Photonic Cellulose Nanocrystal Films as a Platform with Multisensing Functions. *ACS Sustainable Chem. Eng.* **2020**, *8*, 18484−18491.

(195) Yao, K.; Meng, Q.; Bulone, V.; Zhou, Q. Flexible and Responsive Chiral Nematic Cellulose Nanocrystal/Poly(ethylene Glycol) Composite Films with Uniform and Tunable Structural Color. *Adv. Mater.* **2017**, *29*, 1701323.

(196) Querejeta-Fernández, A.; Chauve, G.; Methot, M.; Bouchard, J.; Kumacheva, E. Chiral Plasmonic Films Formed by Gold Nanorods and Cellulose Nanocrystals. *J. Am. Chem. Soc.* **2014**, *136*, 4788−4793.

(197) Xiong, R.; Yu, S.; Smith, M. J.; Zhou, J.; Krecker, M.; Zhang, L.; Nepal, D.; Bunning, T. J.; Tsukruk, V. V. Assembly of Emissive Nanocellulose QD for Chiral Fluorescent Materials. *ACS Nano* **2019**, *13*, 9074−9081.

(198) Yoo, S. J.; Park, Q. H. Metamaterials and Chiral Sensing: A Review of Fundamentals and Applications. *Nanophotonics* **2019**, *8*, 249−261.

(199) Lee, Y. Y.; Kim, R. M.; Im, S. W.; Balamurugan, M.; Nam, K. T. Plasmonic Metamaterials for Chiral Sensing Applications. *Nanoscale* **2020**, *12*, 58−66.

(200) Wang, Y.; Qi, W.; Wang, J.; Li, Q.; Yang, X.; Zhang, J.; Liu, X.; Huang, R.; Wang, M.; Su, R.; He, Z. Columnar Liquid Crystals Self-Assembled by Minimalistic Peptides for Chiral Sensing and Synthesis of Ordered Mesoporous Silica. *Chem. Mater.* **2018**, *30*, 7902−7911.

(201) Ohzono, T.; Yamamoto, T.; Fukuda, J. I. A Liquid Crystalline Chirality Balance for Vapours. *Nat. Commun.* **2014**, *5*, 3735.